



**COMBINED EARTHQUAKE
AND WAVE ACTION
ON OFFSHORE WIND TURBINE
MONOPILE FOUNDATION**

A NUMERICAL INVESTIGATION OF THE
CONTRIBUTION OF HYDRODYNAMIC AND
SOIL RADIATION DAMPING TO THE
RESPONSE OF THE STRUCTURE

STAVROULA KOFOU

Combined Earthquake & Wave action on Offshore Wind Turbine Monopile Foundation

A numerical investigation of the contribution of
hydrodynamic and soil radiation damping to the response
of the structure

by

Stavroula Kofou

to obtain the degree of Master of Science
at the Delft University of Technology,
to be defended publicly on Thursday July 18, 2019 at 13:00 PM.

Student number: 4623053
Project duration: September 17, 2018 – July 18, 2019
Thesis committee: Prof. dr. A. Metrikine, TU Delft, chairman
Dr. ir. H. Hendrikse, TU Delft, supervisor
Ir. W. Luites, Boskalis, supervisor
Dr. ir. A. Tsouvalas, TU Delft

An electronic version of this thesis is available at <http://repository.tudelft.nl/>.

Acknowledgments

First of all, I would like to express my deep gratitude to Professor A. Metrikine for his patient guidance, his useful critiques through my research work and for challenging my thinking to new directions. I owe a very important debt to my university supervisor, Hayo Hendrikse, for his insightful comments and feedback, as well as Pim van der Male for his support during the first months of my work. I would like also to thank Joao Barbosa for providing me with the soil model and for his help, and Alessandro Cabboi for his invaluable suggestions.

Special thanks go to my company supervisor, Wout Luites, who has been a tremendous mentor for me. His encouragement to my work with constructive suggestions and his willingness to devote his time to helping me have been very much appreciated. I would like also to thank the whole design team of Boskalis, and, especially, the manager of the team, Maarten van der Veen, for his support and Marcos Jerez for his great assistance with Python. I would like also to offer my thanks to Panagiotis Antonakas for his precious suggestions and the rest of the colleagues in Boskalis for the friendly environment in the office.

This journey would not have been possible without the encouragement of my family and friends. I am deeply grateful especially to my parents and my brother for supporting me in all my goals and for always believing in me.

Stavroula Kofou
Delft, July 2019

Abstract

The offshore wind industry has been extended over the last years in areas of active seismicity, such as East Asia, where the design of offshore wind turbines becomes significantly challenging, because albeit aerodynamic and hydrodynamic loads mainly act on the offshore structures, earthquake could emerge as a potentially enormous threat.

The demand for reliable and economical design of offshore wind turbine foundations has driven the research for analysis of the structural behaviour under the combined action of loads and the study of the parameters that could influence it.

The present master thesis deals with the dynamic analysis of the response of an offshore wind turbine monopile, one of the most common types of foundations, subjected to the application of hydrodynamic and earthquake loads. This study focuses on the understanding of the dynamic properties contributing to the dissipation of energy experienced by the structure. More specifically, the sources of damping leading to reduction of the structural vibration in time are investigated, of which the numerical determination is considerably uncertain, while emphasizing on the hydrodynamic and the soil damping.

A numerical approach for the estimation of the hydrodynamic viscous damping is presented based on the calculation of the drag coefficient C_D and its dependency on the Reynolds number (Re), the Keulegan-Carpenter number (KC) and the surface roughness (k/D). The drag coefficient, and accordingly the hydrodynamic viscous damping, are derived over the length of the monopile where the waves act, highlighting also the consequences of the changes in diameter and depth.

Furthermore, the soil radiation damping due to the seismic waves is studied by including the interaction of the soil with the structure. Particularly, the supporting soil is modelled around the monopile with frequency-dependent springs and dampers to represent the soil stiffness and damping, respectively. The estimation of the soil coefficients is accomplished by integrating in the model of the structure, an advanced soil model developed by Dr. J. De Oliveira Barbosa, which gives the dynamic impedance function for the desired band of frequencies.

The analysis of the structural response is executed by examining three load cases for the hydrodynamic and earthquake loads. The overall outcome reveals that a noticeable amount of energy is dissipated because of the presence of the soil radiation damping, drawing also the conclusion that the soil-structure interaction should be considered as frequency-dependent during earthquake. Despite the fact that the approach for the estimation of the hydrodynamic viscous damping constitutes a more precise method, its participation in the specific tested cases is limited to the total amount of damping.

Contents

List of Figures	ix
List of Tables	xiii
1 Introduction	1
1.1 Problem Statement	1
1.2 Research Objectives	3
1.3 Scope of the thesis project	3
1.4 Approach	3
1.5 Thesis Outline	3
2 Existing Literature on Damping	5
2.1 Sources of damping on an Offshore Wind Turbine Structure	5
2.1.1 Consideration of damping for Multi-Degree of Freedom systems	6
2.2 Hydrodynamic damping	6
2.2.1 Radiation damping	6
2.2.2 Viscous damping.	7
2.2.3 Drag Coefficient based on the Design Standards DNVGL-RP-C205.	8
3 Theoretical background of Soil-Structure Interaction	11
3.1 Introduction	11
3.2 Methods of Analysis.	12
3.3 Dynamic Impedance Function	12
3.4 Soil Modelling.	13
4 Model Description	15
4.1 Introduction	15
4.2 Beam Theory	16
4.3 Modelling of Soil-Structure Interaction	16
4.4 Formulation of Damping Matrix	18
4.4.1 Hydrodynamic Viscous Damping	18
4.5 Loads	23
4.5.1 Hydrodynamic loads.	23
4.5.2 Earthquake loads	23
4.6 Solution of the Dynamic Problem.	25
4.7 Eigenvalue Problem.	26
4.8 Validation of the solution of the model in the Frequency domain	27
5 Results & Discussion	31
5.1 Dynamic Impedance Function	33
5.2 Hydrodynamic Loading.	35
5.3 Earthquake & Hydrodynamic Loading	42
5.3.1 Response to Earthquake & Regular Waves	42
5.3.2 Response to Earthquake & Irregular Waves.	47
5.4 Discussion regarding the Sensitivity of the Application of FFT	52
6 Conclusions & Recommendations for further research	55
A Details of Structure	57
B Estimation of the Drag Coefficient	61
C Force Spectra	63
Bibliography	65

List of Figures

1.1	Seismic intensity in East Asia Offshore regions	1
1.2	Applied loads on the Offshore Wind Turbine Monopile	2
2.1	Wake amplification factor ψ as a function of KC number for smooth (solid line) and rough (dotted line)	9
2.2	Drag coefficient for fixed circular cylinder for steady flow in critical flow regime, for various roughness values	9
3.1	Description of incident, scattered and reflected waves for SSI in Earthquake Engineering	11
3.2	Soil stiffness & damping as function of frequency	13
4.1	Layout of Offshore Wind Turbine Structure	15
4.2	Modelling of the supporting soil with frequency-dependent springs & dampers	16
4.3	Variation of the diameter along the length of the monopile	19
4.4	Variation of the KC number along the length of the monopile	20
4.5	Variation of the wake amplification factor along the length of the monopile	20
4.6	Variation of the drag coefficient along the length of the monopile	21
4.7	Variation of the standard deviation of the velocity along the length of the monopile	21
4.8	Variation of the hydrodynamic damping coefficient of the velocity along the length of the monopile	21
4.9	Wake amplification factor ψ as a function of KC number for $C_{ds} = 0.65$	22
4.10	Concept of the Response Spectrum	24
4.11	Fixed-bottom monopile	27
4.12	Direct Time Domain Analysis	27
4.13	Direct Frequency Domain Analysis	28
4.14	Soil-structure Interaction Included	28
4.15	Rayleigh damping Included	29
5.1	Response spectrum of the earthquake	31
5.2	Soil Stiffness as a function of frequency for horizontal translational motion	33
5.3	Soil damping as a function of frequency for horizontal translational motion	33
5.4	Soil Stiffness as a function of frequency for rotational motion	34
5.5	Soil damping as a function of frequency for rotational motion	34
5.6	Displacement of node at the top of the tower under the action of irregular waves ($H_s = 5m$, $T_p = 6sec$) with the presence of hydrodynamic and static radiation damping	36
5.7	Amplitude spectrum of the node at the top of the tower under the action of irregular waves ($H_s = 5m$, $T_p = 6sec$) with the presence of hydrodynamic and static radiation damping	36
5.8	Power Spectral Density of the node at the top of the tower under the action of irregular waves ($H_s = 5m$, $T_p = 6sec$) with the presence of hydrodynamic and static radiation damping	36
5.9	Displacement of the node at the mud line under the action of irregular waves ($H_s = 5m$, $T_p = 6sec$) with the presence of hydrodynamic and static radiation damping	37
5.10	Amplitude spectrum of the node at the mud line under the action of irregular waves ($H_s = 5m$, $T_p = 6sec$) with the presence of hydrodynamic and static radiation damping	37
5.11	Power Spectral Density of the node at the mud line under the action of irregular waves ($H_s = 5m$, $T_p = 6sec$) with the presence of hydrodynamic and static radiation damping	37
5.12	Displacement of the node at height +2.00m LAT under the action of irregular waves ($H_s = 5m$, $T_p = 6sec$) with the presence of hydrodynamic and static radiation damping	38
5.13	Amplitude spectrum of the node at height +2.00m LAT under the action of irregular waves ($H_s = 5m$, $T_p = 6sec$) with the presence of hydrodynamic and static radiation damping	38

5.14 Power Spectral Density of the node at height +2.00m LAT under the action of irregular waves ($H_s = 5m$, $T_p = 6sec$) with the presence of hydrodynamic and static radiation damping	38
5.15 Displacement of the node at the mud line under the action of irregular waves ($H_s = 5m$, $T_p = 6sec$) with static radiation damping (hydrodynamic damping is not included)	39
5.16 Amplitude spectrum of the node at the mud line under the action of irregular waves ($H_s = 5m$, $T_p = 6sec$) with static radiation damping (hydrodynamic damping is not included)	39
5.17 Power Spectral Density of the node at the mud line under the action of irregular waves ($H_s = 5m$, $T_p = 6sec$) with static radiation damping (hydrodynamic damping is not included)	39
5.18 Displacement of the node at height +2.00m LAT under the action of irregular waves ($H_s = 5m$, $T_p = 6sec$) with static radiation damping (hydrodynamic damping is not included)	40
5.19 Amplitude spectrum of the node at height +2.00m LAT under the action of irregular waves ($H_s = 5m$, $T_p = 6sec$) with static radiation damping (hydrodynamic damping is not included)	40
5.20 Power Spectral Density of the node at height +2.00m LAT under the action of irregular waves ($H_s = 5m$, $T_p = 6sec$) with static radiation damping (hydrodynamic damping is not included)	40
5.21 Displacement of the node at the mud line under the action of irregular waves ($H_s = 5m$, $T_p = 6sec$) with the presence of hydrodynamic and frequency-dependent radiation damping	41
5.22 Amplitude spectrum of the node at the mud line under the action of irregular waves ($H_s = 5m$, $T_p = 6sec$) with the presence of hydrodynamic and frequency-dependent radiation damping	41
5.23 Power Spectral Density of the node at the mud line under the action of irregular waves ($H_s = 5m$, $T_p = 6sec$) with the presence of hydrodynamic and frequency-dependent radiation damping	41
5.24 Acceleration of the node at the top of the tower under the action of regular waves ($H_s = 0.3m$, $T_p = 5sec$) & earthquake loads with the presence of hydrodynamic and static radiation damping	43
5.25 Acceleration Amplitude Spectrum of the node at the top of the tower under the action of regular waves ($H_s = 0.3m$, $T_p = 5sec$) & earthquake loads with the presence of hydrodynamic and static radiation damping	43
5.26 Power Spectral Density of the node at the top of the tower under the action of regular waves ($H_s = 0.3m$, $T_p = 5sec$) & earthquake loads with the presence of hydrodynamic and static radiation damping	43
5.27 Acceleration of the node at the mud line under the action of regular waves ($H_s = 0.3m$, $T_p = 5sec$) & earthquake loads with the presence of hydrodynamic and static radiation damping	44
5.28 Acceleration Amplitude Spectrum of the node at the mud line under the action of regular waves ($H_s = 0.3m$, $T_p = 5sec$) & earthquake loads with the presence of hydrodynamic and static radiation damping	44
5.29 Power Spectral Density of the node at the mud line under the action of regular waves ($H_s = 0.3m$, $T_p = 5sec$) & earthquake loads with the presence of hydrodynamic and static radiation damping	44
5.30 Acceleration of the node at the top of the tower under the action of regular waves ($H_s = 0.3m$, $T_p = 5sec$) & earthquake loads with the presence of hydrodynamic and frequency-dependent radiation damping	45
5.31 Acceleration Amplitude Spectrum of the node at the top of the tower under the action of regular waves ($H_s = 0.3m$, $T_p = 5sec$) & earthquake loads with the presence of hydrodynamic and frequency-dependent radiation damping	45
5.32 Power Spectral Density of the node at the top of the tower under the action of regular waves ($H_s = 0.3m$, $T_p = 5sec$) & earthquake loads with the presence of hydrodynamic and frequency-dependent radiation damping	45
5.33 Acceleration of the node at the mud line under the action of regular waves ($H_s = 0.3m$, $T_p = 5sec$) & earthquake loads with the presence of hydrodynamic and frequency-dependent radiation damping	46
5.34 Acceleration Amplitude Spectrum of the node at the mud line under the action of regular waves ($H_s = 0.3m$, $T_p = 5sec$) & earthquake loads with the presence of hydrodynamic and frequency-dependent radiation damping	46
5.35 Power Spectral Density of the node at the mud line under the action of regular waves ($H_s = 0.3m$, $T_p = 5sec$) & earthquake loads with the presence of hydrodynamic and frequency-dependent radiation damping	46
5.36 Acceleration of the node at the top of the tower under the action of irregular waves ($H_s = 5m$, $T_p = 6sec$) & earthquake loads with the presence of hydrodynamic and static radiation damping	48

5.37 Acceleration Amplitude Spectrum of the node at the top of the tower under the action of irregular waves ($H_s = 5m$, $T_p = 6sec$) & earthquake loads, with the presence of hydrodynamic damping and static radiation damping	48
5.38 Power Spectral Density of the node at the top of the tower under the action of irregular waves ($H_s = 5m$, $T_p = 6sec$) & earthquake loads with the presence of hydrodynamic and static radiation damping	48
5.39 Acceleration of the node at the mud line under the action of irregular waves ($H_s = 5m$, $T_p = 6sec$) & earthquake loads with the presence of hydrodynamic and static radiation damping	49
5.40 Acceleration Amplitude Spectrum of the node at the mud line under the action of irregular waves ($H_s = 5m$, $T_p = 6sec$) & earthquake loads, with the presence of hydrodynamic damping and static radiation damping	49
5.41 Power Spectral Density of the node at the mud line under the action of irregular waves ($H_s = 5m$, $T_p = 6sec$) & earthquake loads with the presence of hydrodynamic and static radiation damping	49
5.42 Acceleration of the node at the top of the tower under the action of irregular waves ($H_s = 5m$, $T_p = 6sec$) & earthquake loads with the presence of hydrodynamic and frequency-dependent radiation damping	50
5.43 Acceleration Amplitude Spectrum of the node at the top of the tower under the action of irregular waves ($H_s = 5m$, $T_p = 6sec$) & earthquake loads, with the presence of hydrodynamic damping and frequency-dependent radiation damping	50
5.44 Power Spectral Density of the node at the top of the tower under the action of irregular waves ($H_s = 5m$, $T_p = 6sec$) & earthquake loads with the presence of hydrodynamic and frequency-dependent radiation damping	50
5.45 Acceleration of the node at the mud line under the action of irregular waves ($H_s = 5m$, $T_p = 6sec$) & earthquake loads with the presence of hydrodynamic and frequency-dependent radiation damping	51
5.46 Acceleration Amplitude Spectrum of the node at the mud line under the action of irregular waves ($H_s = 5m$, $T_p = 6sec$) & earthquake loads, with the presence of hydrodynamic damping and frequency-dependent radiation damping	51
5.47 Power Spectral Density of the node at the mud line under the action of irregular waves ($H_s = 5m$, $T_p = 6sec$) & earthquake loads with the presence of hydrodynamic and frequency-dependent radiation damping	51
5.48 Force spectrum for regular waves ($H_s = 5m$, $T_p = 6sec$)	52
5.49 Zoomed force spectrum for regular waves ($H_s = 5m$, $T_p = 6sec$)	52
C.1 Force spectrum for irregular waves ($H_s = 5m$, $T_p = 6sec$)	63
C.2 Force spectrum for regular waves ($H_s = 0.3m$, $T_p = 5sec$) and earthquake	63
C.3 Force spectrum for irregular waves ($H_s = 5m$, $T_p = 6sec$) and earthquake	64

List of Tables

4.1	Approximate Values of the Natural Frequencies	26
A.1	Material Properties of the Structure	57
A.2	Details of the Foundation above mud line	57
A.3	Details of the Foundation below mud line	58
A.4	Details of the Tower	59
B.1	Values for the variation of the drag coefficient	61

Nomenclature

β	Stokes parameter	[-]
ν	Fluid kinematic viscosity	$[m^2/s]$
ω	angular frequency	$[rad/sec]$
ψ	Wake Amplification Factor	[-]
ρ	Density	$[kg/m^3]$
σ_u	Standard deviation of the velocity	$[kg/m^3]$
ζ	Damping ratio	[-]
a	Acceleration	$[kg/m^3]$
C	Damping Matrix	
C_D	Drag coefficient	[-]
C_M	Inertia coefficient	[-]
D	Diameter	$[m]$
E	Young modulus	$[Pa]$
F	Force Matrix	
f_D	Drag term of Morison Equation	
FE	Finite Element	
FFT	Fast Fourier Transform	
$H(\omega)$	Transfer function	
H_s	Significant wave height	$[m]$
$IFFT$	Inverse Fast Fourier Transform	
Im	Imaginary part of a complex number	
K	Stiffness Matrix	
k	Surface roughness	$[m]$
KC	Keulegan-Carpenter number	[-]
M	Mass matrix	
$MDoF$	Multi Degree of Freedom	
$PMLs$	Perfectly Matched Layers	
Re	Real part of a complex number	
Re	Reynolds number	[-]
T_p	Wave period	$[s]$

U	Maximum orbital particle velocity	[m/s]
u	Total flow velocity	[m/s]
u	Velocity	[m/s]
z	Depth	[m]
PSD	Power Spectral Density	
SSI	Soil-Structure Interaction	

Introduction

Over the past decade, the interest in renewable energy has led to an extensive development of offshore wind farms. The good quality of the wind and the available space at the sea allow the utilization of large-scale turbines, contributing significantly to the energy production. The energy policy, which aims at the reduction of CO₂ emissions and the mitigation of climate change, is adopted by a continuously increasing number of countries. Europe is dominant in the global market concerning the offshore wind energy and has already established the target to produce 40 GW via this technique by 2020. However, the market is also extending outside Europe. Asia focuses on the energy production based on offshore wind as well, with various operating and under construction projects. It should be pointed out that the Taiwanese government aims to achieve 5.5 GW via offshore wind by 2025 [8] and to cover 20% of the country's supply from renewable sources [3].

1.1. Problem Statement

The increasing demand in offshore wind energy has also motivated the research for an appropriate design of the offshore wind structures, given the variable regional conditions. Based on an environmental point of view, two important parameters for the design are the *aerodynamic wind load* and the *ocean wave load*. However, in areas of active seismicity, *earthquake load* consists a large concern.

The present master thesis focuses mainly on the design of offshore wind structures in the offshore coast of Taiwan, namely Taiwan Strait, which is positioned in an active tectonic area of magnitudes reaching values larger than 7, as it is depicted in the Figure 1.1 [29]. The fact that the earthquake load could be a considerable potential threat for the offshore wind turbine structures highlights the significance of introducing a seismic analysis to their design.

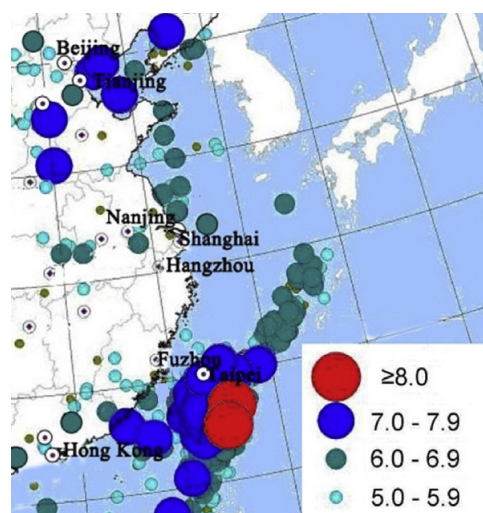


Figure 1.1: Seismic intensity in East Asia Offshore regions

Nonetheless, performing a seismic analysis and addressing the forces acting on structures based on the earthquake loads without accounting the effect of the wave and/or wind loads could result in underestimation of the structural response, considering the dynamic aspect of the problem. The investigation of the joint action of seismic and wave loads is really important for understanding the effects of it on the behaviour of the structure.

Zheng et al. [29] highlight that collected data for the most recent five decades in Asia showed that several strong earthquakes have occurred during the winter or spring season in which the occurrence probability of moderate or even severe sea states was high. That could be interpreted as a threat for the offshore wind structures due to the joint earthquake and wave action, although a damage due to this combination has not reported yet.

The offshore wind turbines are flexible structures and their resonance frequencies could possibly be close to the excitation frequencies of the environmental loads. In order to avoid conservatism during the load calculation and the design phase, which could possibly lead to additional costs, the structural response should be analyzed using reliable estimations of the dynamic properties of the structure [9]. A small change on the damping of the structure could possibly lead to a great change in the response. A complete understanding of the forms contributing to the dissipation of the energy experienced by the structure is crucial for the evaluation of its behaviour. The interest is focused on the hydrodynamic and soil damping.

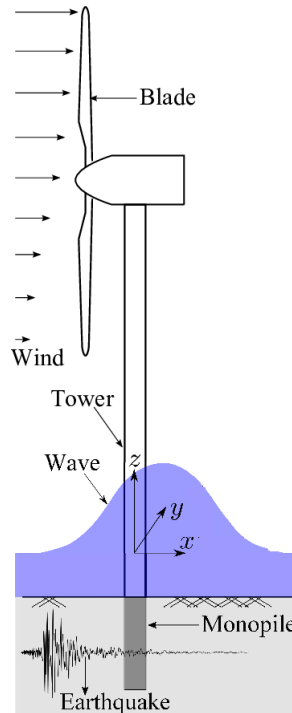


Figure 1.2: Applied loads on the Offshore Wind Turbine Monopile

It should be highlighted that Sarpkaya discusses in "Wave Forces on Offshore Structures" [20] about the fundamental as well as practical problem of the estimation of the hydrodynamic damping, referred especially to the hydrodynamic viscous damping. It is stated in [20] that the measurement of the hydrodynamic damping is applicable, though its prediction numerically is rather difficult.

Moreover, research concerning the earthquake action reveals that during the seismic excitation, the soil affects the behaviour of the structure by dissipating the energy through the seismic waves carried away from the structure. Due to the phenomenon, the response of the structure is considered as frequency-dependent [16].

1.2. Research Objectives

The present master thesis is devoted to the investigation of the combined action of earthquake and wave loads on offshore wind structures in areas of active seismicity. The problem is approached from a dynamic point of view, in order to understand the response of the structures under them.

One of the main objectives is the numerical approach for the estimation of the hydrodynamic damping including the dependency of the Reynolds number, the KC number and the surface roughness and the variation of the drag coefficient with the height. Moreover, the inclusion of the soil radiation damping by modelling the soil-structure interaction with frequency-dependent springs and dampers is an important part of this thesis, as well as the investigation of the significance of accounting the soil as frequency-dependent.

Furthermore, the composition of the total damping matrix of the system, instead of making use of a representative one, and the comparison of contribution of the sources to the total damping are executed. The ability of the hydrodynamic and soil damping to dissipate the energy of the structure under the action of the loads is also studied.

1.3. Scope of the thesis project

Although the problem of the combined loads and the uncertainty about the behaviour of the structure to them concerns all the types of offshore wind turbine foundations, for this project a model simulation of a monopile is chosen. Monopile is currently the most common foundation in the offshore wind worldwide, as it offers an economic solution and it is relatively simple for fabrication and installation. Thus, it is considered logical firstly to study and carry out the analysis on this type of foundation, aiming at the complete understanding of its response to wave and earthquake loads, before proceeding with more complex types of foundation.

The present project aims at studying the dynamic analysis of the offshore wind turbine foundation under earthquake and hydrodynamic loads, which are based on random generated data and not on real measurements, without considering the aerodynamic loads. It is also assumed that no axial loads act on the structure.

The investigation of the sources of damping focuses on the hydrodynamic and soil damping, two parameters that include a lot of uncertainty in their estimation. However, the aerodynamic damping which is considered as dominant in the dissipation of energy of the structure is not added, in order to distinguish the contribution of the other types of damping more easily.

1.4. Approach

The structure is modelled as a beam based on the Euler-Bernoulli theory, with a concentrated mass on the top representing the rotor nacelle assembly. The Finite Element Method is used to divide the structure into elements. The problem is considered as two-dimensional. Load cases with hydrodynamic and earthquake loads acting on the structure are studied, where the differences on the dynamic properties of the structure are analyzed.

A numerical approach for the estimation of the hydrodynamic damping is performed, based on the dependency of the drag coefficient on parameters such as the KC number which is presented on the DNVGL-RP-C205 Design Standards [10].

The soil-structure interaction is modelled with frequency-dependent springs and dampers to capture the totally frequency-dependent phenomenon. The soil stiffness and damping coefficients are derived by the dynamic impedance function, which was estimated by including a soil model developed by Dr. J. De Oliveira Barbosa. As the information for the soil is frequency-dependent, the solution of the dynamic problem is executed with direct frequency analysis considering all the excitation frequencies.

1.5. Thesis Outline

The present Master Thesis is divided into the following sections:

In Sections 2 & 3, a theoretical framework based on the sources of damping and the soil-structure interaction, respectively, are presented.

In Section 4 the numerical model is presented, including the approach for the hydrodynamic and the soil damping.

Section 5 shows the analysis of the structure under the tested load cases, as well as the discussion of the results.

In Section 6 the conclusions and the recommendations for further research are shown.

2

Existing Literature on Damping

2.1. Sources of damping on an Offshore Wind Turbine Structure

Generally, the understanding of the forms contributing to the dissipation of energy experienced by an offshore wind turbine structure is really important, as they lead to a decay of its motion, and subsequently to a reduction of the fatigue damage during its lifetime. In the study of a structural system, quantities such as the mass and the stiffness can be easily calculated, however the damping, which leads to a reduction of the vibration amplitude in time, is a very uncertain quantity that cannot always be considered sufficiently as there is a difficulty on the determination of it through numerical tools. Various researches focus on the different sources of the damping, as well as how they can be included in the formulation of the dynamic problem.

There are various forms of damping that a wind turbine structure experiences during its presence in the offshore environment and originate from various sources. The total damping of the structural system consists of the combination of aerodynamic, structural, hydrodynamic, soil and due to additional dampers damping.

$$\zeta_{\text{total}} = \zeta_{\text{aero}} + \zeta_{\text{struc}} + \zeta_{\text{hydro}} + \zeta_{\text{soil}} + \zeta_{\text{dampers}} \quad (2.1)$$

The **aerodynamic damping** (ζ_{aero}) comes from the interaction of the wind turbine with air during the vibration of the wind support structure. The aerodynamic damping effect is part of an important physical phenomenon for wind turbines called aeroelasticity [22]. More specifically, the vibration of the wind turbine components is strongly coupled to the system's aerodynamic mechanisms.

It should be mentioned that a very large amount of aerodynamic damping is achieved when the turbine is on the production state. In a non-production state, such as in cases as in perpendicular rotor direction and in wind-wave misalignment, no or negligible amount of aerodynamic damping is present [11].

It is important to distinguish the operational regime in which the load analysis is executed (power production, start-up and shut-down etc.) and determine if the aerodynamic damping should be taken into account.

The **structural damping** (ζ_{struc}) originates from the internal friction of a material that transforms vibrational energy into heat [22].

The **hydrodynamic damping** (ζ_{hydro}) is of special interest for the Offshore Engineering, as it requires a complete understanding of the flow around the structure. It consists of two sources, the radiation and the viscous damping, which are explained further in Section 2.2, as they are of special interest for the present study.

To assess the amount of the **soil damping** (ζ_{soil}) that contributes to the energy dissipation of the structure, it is crucial to study its interaction with the soil. In general, the soil damping consists of the radiation, the hysteretic (material) and the much smaller pore fluid material. These sources of damping are discussed in Chapter 3, where the soil-structure interaction is presented.

Additionally, the damping (ζ_{dampers}) due to constructive devices, such as the tower dampers, that can contribute to the total damping of the system.

2.1.1. Consideration of damping for Multi-Degree of Freedom systems

In the equation of motion the damping matrix is formulated, which is proportional to the velocity, resulting to a damping force. The formulation of the damping matrix can be more easily achievable in cases of simple structures, where usually the damping ratio for every vibrational mode is found. However, for larger structures with many structural elements it is difficult to approximate the damping specifically for every vibration mode. For that reason, many forms of damping matrices in MDoF systems are introduced, such as the Rayleigh damping and special cases of it as the mass proportional and the stiffness proportional damping.

The Rayleigh damping is widely used in FE packages, as it combines the two cases of mass and stiffness proportionality. It results in a diagonal matrix which can be easily applied in modal analysis and it is identified by two modes. However, there are systems where the Rayleigh damping cannot be used, for instance when the soil-structure interaction is taken into account and there are different amounts of damping in the soil and the structure [26]. In cases also that the classical modal analysis cannot be applied, it is difficult to continue with the diagonal matrix based on the Rayleigh damping.

2.2. Hydrodynamic damping

An extended literature review was executed in order to fully comprehend the different parameters concerning the problem and include the executed studies based on them up until now.

Hydrodynamic damping is an important parameter contributing to the decrease of the amplitude of the oscillation of the structure. It is a fundamental problem for the derivation of reliable responses of the structure, because its estimation contains a large level of uncertainty.

The total hydrodynamic damping arises from two main sources, the radiation and the viscous damping.

2.2.1. Radiation damping

Radiation damping is the damping from of the wave creation, because of the vibration of the structure. The force on the structure due to the generation of the waves F_w is equal to the sum of a component in phase with the velocity of the body and a component in phase with the acceleration of the body [15], as it is shown in the following equation:

$$F_{w_i} = - \sum_{j=1}^6 (\mu_{ij} \ddot{x}_j + \lambda_{ij} \dot{x}_j), \text{ for } i = 1, 2, \dots, 6 \quad (2.2)$$

where:

\dot{x}_j : velocity of the body

\ddot{x}_j : acceleration of the body

j : concerns the 6 components of the motion of the structure (surge, sway, heave, roll, pitch, yaw)

μ_{ij} & λ_{ij} : added mass and damping due to wave creation

The equation of motion of the structure, taking into account the force due to the wave generation is:

$$F_{w_i} = (m_{ij} + \mu_{ij}) \ddot{x}_j + \lambda_{ij} \dot{x}_j + \kappa_{ij} x_{ij} \quad (2.3)$$

where:

m_{ij} : mass of the system

κ_{ij} : stiffness of the system

The term λ_{ij} expresses the radiation damping and it can be estimated as:

$$\lambda_{ij} = \frac{i\rho}{\omega} \int_{S_0} \text{Re}[\phi_j^{(f)}] \frac{\partial \phi_i^{(f)}}{\partial n} dS \quad (2.4)$$

where:

ρ : fluid density

ω : frequency

S: volume of the body per unit length $\phi_j^{(f)}$: is the velocity potential due to the body motion

2.2.2. Viscous damping

Viscous damping is the damping due to the viscous drag forces, experienced by the structure that is vibrating in a viscous fluid. It is measurable, but it cannot be predicted easily. For various engineering purposes, experimentally measured quantities are used. However, this does not lead to a complete understanding behind the physics of the specific phenomenon. It is significant to highlight that the viscous drag forces depend on the nature of the flow around the body that is oscillating and on the boundary layers. More specifically, the very thin layer of the wall of the body and the possible instabilities of it make the quantity of the viscous damping difficult to be predicted. The viscous damping is expressed with the drag coefficient, which depends on the following parameters:

- the *Reynolds number* (Re), a dimensionless quantity used to predict the different flow patterns. It is defined as:

$$Re = \frac{u * D}{\nu} \quad (2.5)$$

- the *Keulegan-Carpenter number* (KC), a dimensionless quantity used to describe the relative importance of drag forces over inertia forces for bluff objects in an oscillatory fluid flow. It is defined as:

$$KC = \frac{U * T}{D} \quad (2.6)$$

- the *roughness* of the surface of the structure, which is expressed with the non-dimensional roughness k/D .

The *Stokes parameter* $\beta (= Re/KC)$ is also used for oscillatory flows, because it is considered more appropriate than Reynolds number to express the viscosity. It is important for the structures to undergo a dynamic excitation in a range of flow parameters defined by very small KC numbers and very large Stokes parameters, which means large rates of diffusion of vorticity.

The past experimental work for the estimation of the hydrodynamic damping is described by Sarpakaya [20].

Stokes [24] set the basis by performing the first solutions for the damping force for a laminar, unseparated and stable flow around an oscillating circular cylinder with small amplitude, valid for $KC \ll 1$ and $\beta \gg 1$.

$$C_D = \frac{24}{Re} \left(1 + \frac{1}{2} \sqrt{\pi \frac{Re}{KC}} \right) = \frac{24}{Re} \left(1 + \frac{1}{2} \sqrt{\pi \beta} \right) \quad (2.7)$$

As it can be seen from the equation, the dependence of drag coefficients on the parameters mentioned before is clear. This calls attention to the presence and the effect of the viscosity of the fluid and the fact that it cannot be extracted from a fluid in motion.

Wang [28] extended Stokes' classical solutions to higher terms to include the "in-phase" and "out-of-phase" components of the force with the motion. His result was useful for the estimation of C_d . However, that was not valid in conditions where the boundary layer is turbulent, or where the flow is three dimensional [15].

$$C_D = \frac{3\pi^3}{2KC} \left[(\pi\beta)^{-1/2} + (\pi\beta)^{-1} - 6(\pi\beta)^{-3/2} + \dots \right] \quad (2.8)$$

It should be mentioned that for very large values of β , the drag coefficient is reduced to just the first term in the previous equation:

$$C_D = \frac{3\pi^3}{2KC} (\pi\beta)^{-1/2} \quad (2.9)$$

This leads to the following expression:

$$\{KC * C_D \sqrt{\beta}\}_{S-W} = 26.24 \quad (2.10)$$

Taking into account the previous expression, but also based on experimental tests it can be pointed out that for KC numbers below a certain value and depending on the β values, the drag coefficient is inversely proportional to KC.

Bearman & Russel [5] proposed the following relationship for the drag coefficient for very high values of KC (KC larger than 5).

$$C_D = \frac{2 * 26.24}{KC \sqrt{\beta}} + 0.08 * KC \quad (2.11)$$

For small values of KC, it can be seen that the expression becomes equal to (2.10).

After an extensive review of the models by Sarpkaya [20], it is concluded that the degree of empiricism increases as the Reynolds number, separation, convective accelerations and the three-dimensionality of the wake increase. Although, the time-dependent fluid force as a function of velocities and accelerations is expressed with non-linear motions for numerical models, the problem of separation and turbulence already exists.

2.2.3. Drag Coefficient based on the Design Standards DNVGL-RP-C205

In the Design Standards concerning the environmental conditions and environmental loads: DNVGL-RP-C205 [10], the drag coefficient C_D is referred as the hydrodynamic damping coefficient. Its dependence on the previously mentioned parameters, Reynolds number, KC number and surface roughness (expressed as $\Delta = k/D$), is also highlighted.

The relationship between drag coefficient and non-dimensional surface roughness is expressed as:

$$C_{DS}(\Delta) = \begin{cases} 0.65, & \Delta < 10^{-4} (\text{smooth}) \\ (29 + 4 * \log_{10}(\Delta))/20, & 10^{-4} < \Delta < 10^{-2} \\ 1.05, & \Delta > 10^{-2} (\text{rough}) \end{cases} \quad (2.12)$$

The previous expression can be applied for regular and irregular wave analysis.

The variation of the drag coefficient concerning the KC number for smooth and rough circular cylinders, can be calculated by:

$$C_D = C_{DS}(\Delta) * \psi(K_C) \quad (2.13)$$

where:

$\psi(K_C)$ is the wake amplification factor.

For small values of KC ($K_C < 12$), the wake amplification factor can be estimated as:

$$\psi(K_C) = \begin{cases} C_\pi + 0.10(K_C - 12), & 2 \leq K_C < 12 \\ C_\pi - 1.00, & 0.75 \leq K_C < 2 \\ C_\pi - 1.00 - 2.00(K_C - 0.75), & K_C \leq 0.75 \end{cases} \quad (2.14)$$

where:

$$C_\pi = 1.50 - 0.024 * (12/C_{DS} - 10) \quad (2.15)$$

In Figure 2.1, the wake amplification factor as a function of the KC number and the C_{DS} coefficient for smooth and rough surface of the cylinder is presented.

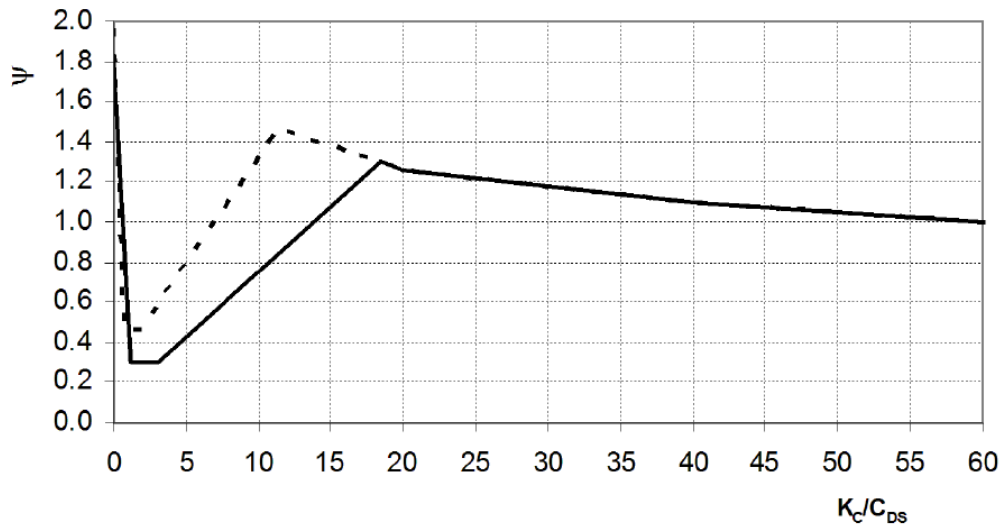


Figure 2.1: Wake amplification factor ψ as a function of KC number for smooth (solid line) and rough (dotted line)

Figure 2.2 depicts the variation of the drag coefficient for different surface roughness values.

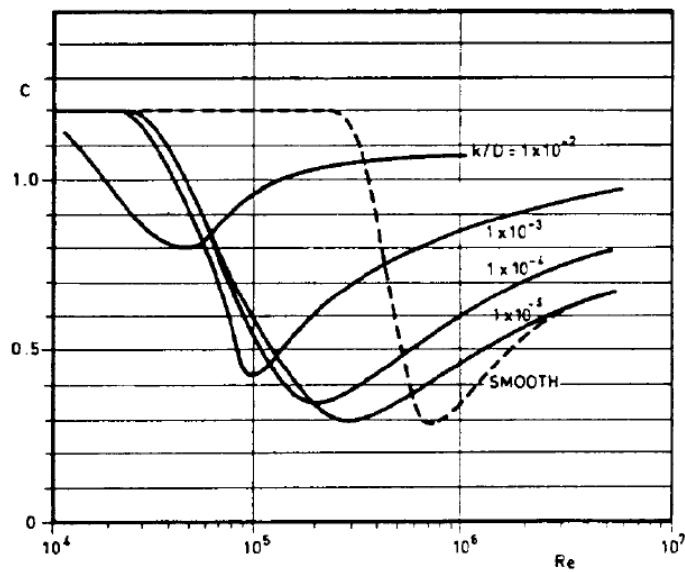


Figure 2.2: Drag coefficient for fixed circular cylinder for steady flow in critical flow regime, for various roughness values

3

Theoretical background of Soil-Structure Interaction

3.1. Introduction

Soil-Structure Interaction (SSI) describes the behaviour of the structure together with the supporting soil under the action of loads. For the Earthquake Engineering this phenomenon could be considered tremendously important as, by not taking that into account, errors in the analysis of the response of the structure could emerge. During earthquake, inertia forces are developed, which lead to base shears and bending moments at the interface of the structure with the foundation. Considering the interaction of the structure and the supporting soil makes the structural system more flexible and leads to smaller displacements and rotations that could be neglected compared to the ones above the mud line.

In Earthquake Engineering the SSI differs compared to cases of other fields, because the seismic loads do not originate from the structure towards the soil, but from the soil towards the structure. During Earthquake, the waves excite the foundation of the structure, which in turn vibrates and changes the soil motion beneath them with the radiation of waves that carry the energy away [26], as it is shown in Figure 3.1.

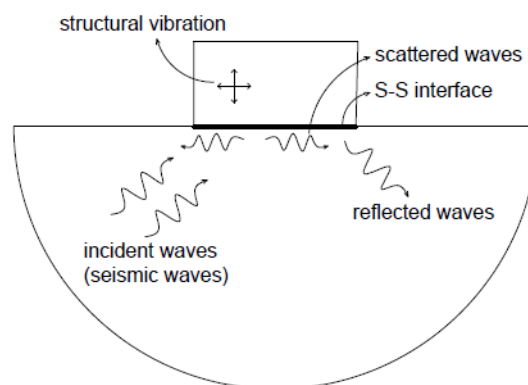


Figure 3.1: Description of incident, scattered and reflected waves for SSI in Earthquake Engineering

Due to the presence of the earthquake excitation, the soil influences the response of the structure in various ways. In the absence of the structure, the seismic event creates a free motion in the soil which is different from the case when the structure is present [19]. In the presence of the structure at the top of the soil, the free-field motion changes to another seismic input. This phenomenon is called *kinematic interaction* and it is caused by the fact that the equilibrium that should be satisfied at the structure-soil interface is not the one of a stress-free surface which was the basis for the determination of the original site response spectra or seismic input motions provided by the seismologist [26]. The intensity of the phenomenon depends on

various parameters, such as the geometry of the structure, the type of the foundation and the kinematics of the incident free field motion.

The dynamic coupling of the structure and the supporting soil causes another phenomenon, which is called *inertial interaction*, because the structure lying above the soil is dynamically excited.

The soil contributes also to the dissipation of the energy through the radiation of the seismic waves away from the structure and through the inelastic deformation [16]. However, when the deformation of the soil is non-linear, the amount of the radiation damping can be limited, because the plastic waves cannot dissipate efficiently the energy away.

The inertial phenomenon and the dissipation of the energy are considered significant properties of the soil-structure interaction system in making the dynamic response of the foundation frequency-dependent.

3.2. Methods of Analysis

The level of the complexity of the analysis of the SSI problem depends on the purpose of the engineering calculation and the available information. Generally, there are two approaches for the solution of the problem, which are explained briefly:

1. *The Direct Approach,*

in which the soil and the structure are modelled together as part of the soil model using the Finite Element Method. It can be implemented for both linear and non-linear cases and it accounts automatically the interaction of the structure with the soil. However, the method is very extensive computationally and requires full description of the soil domain.

2. *The Substructure Method,*

in which the coupled system of the structure and the soil is separated in two different subsystems, i.e. the foundation-soil system and the superstructure. The response of the system is calculated independently for the two systems and the response of the total system is determined by making use of the superposition's theorem. This method is simpler computationally, but it is applied only for linear analysis.

It should be mentioned that the choice of the method that will be followed depends on the requirements of every case for simpler or more detailed representation of the model.

3.3. Dynamic Impedance Function

For the dynamic soil-structure interaction an important step is the calculation of the relationship between the force and the displacement at all the nodes at the foundation level. Usually the assumption of a rigid foundation on a half infinite soil is considered. If an harmonic force $F(t)$ is applied at each node of soil-structure interaction, giving a steady-state displacement $u(t)$, then the ratio between them is called *dynamic impedance function* or *dynamic soil stiffness matrix* and it could be calculated for every excitation frequency. The force and the displacement can be written in a complex form:

$$F_z(t) = \tilde{F}e^{i\omega t} \quad (3.1)$$

$$u_z(t) = \tilde{u}e^{i\omega t} \quad (3.2)$$

Where: \tilde{F} and \tilde{u} are also complex-valued numbers

The dynamic impedance function is then equal to:

$$\tilde{K}(\omega) = \frac{F_z(t)}{u_z(t)} \quad (3.3)$$

Where:

$$\tilde{K}(\omega) = Re(\tilde{K}(\omega)) + iIm(\tilde{K}(\omega)) \quad (3.4)$$

Or:

$$\tilde{K}(\omega) = \hat{K}(\omega) + i\omega\tilde{C}(\omega) \quad (3.5)$$

It should be noted that the real part of the dynamic stiffness represents the inertia and stiffness of the supporting soil. The imaginary part component reflects two types of damping, the radiation and the material damping. The first one is generated by the energy carried away by waves and the second one is due to the hysteretic soil behaviour.

The dynamic soil matrix can be derived from analytical or semi-analytical models, finite element or boundary element models or alternatively, through in-situ measurements and experiments.

In Figure 3.2 [19], the behaviour of the stiffness and the damping as a function of the frequency is presented:

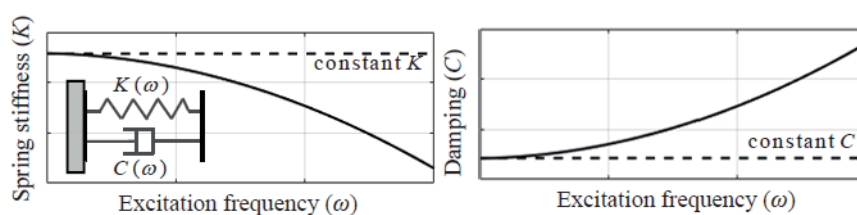


Figure 3.2: Soil stiffness & damping as function of frequency

3.4. Soil Modelling

There are various ways of modelling the soil together with the structure, considering also the type of the foundation (shallow, fully embedded etc.). Focusing on the piles, one of the most common approaches is the Winkler model, which is composed by a distribution of linear/non-linear non-connected springs along the pile and the deflection at any point of the soil in contact with the pile is linearly related to the corresponding contact pressure at that point [16].

For the derivation of the impedance function, one approach that can be used is the modification of the classical Winkler model, known as *modified Winkler method*. In that case, the springs are characterized as non-linear and frequency-dependent, and dampers, also frequency-dependent, can be included in parallel to represent the energy dissipation.

It should be stated that in many cases the use of frequency-dependent springs and dampers may not be chosen, because it gives information in the frequency domain and the most classical approaches analyze the problem in the time domain. However, the original soil response is frequency-dependent and the excitation of the earthquake is also broadband. The solution of the problem only in one frequency could possibly lead to inaccurate results for the response of the system and the soil coefficients.

4

Model Description

4.1. Introduction

For the model simulation, an offshore design tool, which was developed in Boskalis, is used. The tool is based on the programming language Python and aims at modelling the dynamic behaviour of offshore structures under various loads. The model is based on the Finite Element Method.

Since the Finite Element Method is utilized, the whole structure (foundation and tower) is composed by nodes and elements. The mass of the nacelle and the rotor are considered as concentrated mass at the top node of the tower. As the specific project focuses on the hydrodynamic and earthquake loads acting on the structure laterally, every element is modelled as a beam.

The total modelled structure consists of the wind turbine, the tower, the transition piece and the foundation, as presented in Figure 4.1. The surrounding soil was also modelled with frequency-dependent springs and dampers. A 10MW reference turbine is considered. The properties of the structure are presented in detail in Appendix A.

It should be also mentioned that the problem is examined as two-dimensional considering the x and z direction according to the notation presented in Figure 4.1.

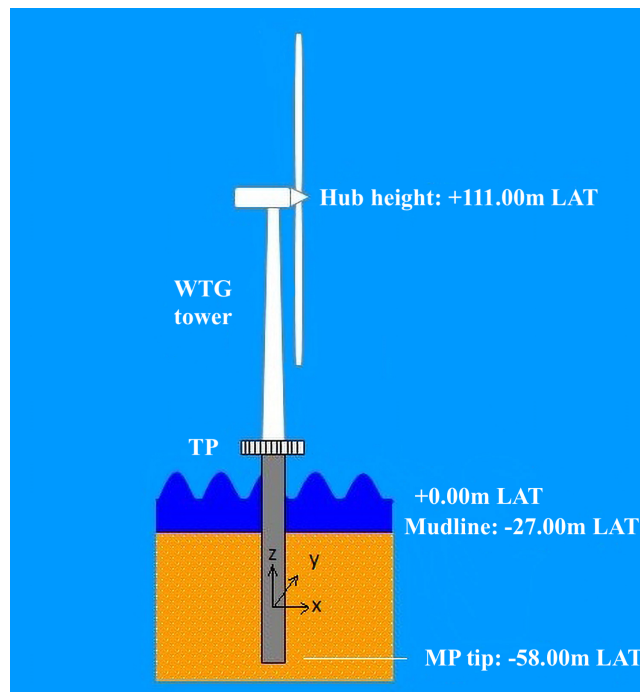


Figure 4.1: Layout of Offshore Wind Turbine Structure

4.2. Beam Theory

The structural mass and stiffness contributions to the global mass $[M]$ and stiffness $[K]$ matrices are calculated according to the Euler-Bernoulli beam theory. This specific theory is based on the kinematic assumption that for deformations of the beam the section remains plane and perpendicular to the neutral axis. The global mass and stiffness matrices are obtained by assembling the individual element contributions.

4.3. Modelling of Soil-Structure Interaction

The interaction of the structure with the soil is included through frequency-dependent springs and dampers along the length of the monopile below the mud line (Figure 4.2), representing the soil stiffness and damping, respectively. In such manner, the phenomenon of the frequency-dependent dissipation of the energy through the soil is captured.

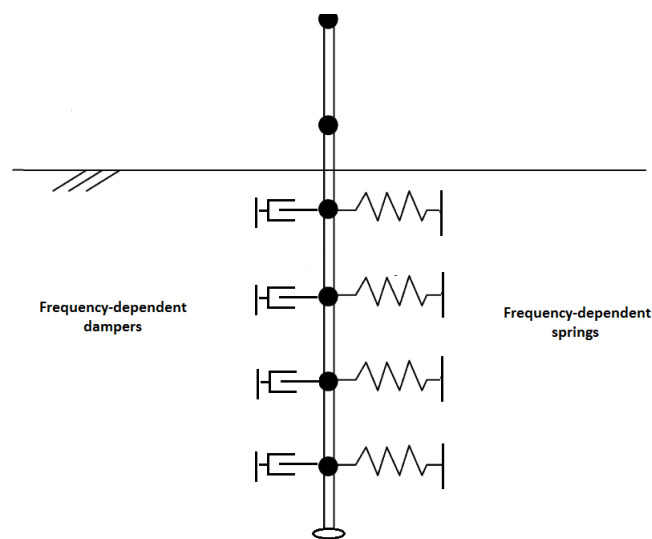


Figure 4.2: Modelling of the supporting soil with frequency-dependent springs & dampers

The estimation of the soil coefficients for various frequencies, as it is described in Chapter 3, requires a full study of the soil profile and it is rather complex computationally. For this purpose, the inclusion of the frequency-dependent springs and dampers was executed through a separate MATLAB based FE model by Dr. J. De Oliveira Barbosa [27], which was connected with the Python Design Tool.

The soil model estimates the dynamic stiffness matrix for the desired range of frequencies [27]. More specifically, it considers the monopile as axially symmetric, decomposing the 3-D problem into 2-D, where the soil and the pile are modelled as Finite Elements. The volume corresponding to the pile wall is removed. An horizontal force and a bending moment around y-axis are applied at each node of the embedded pile, assuming that they have uniform distribution around the perimeter of the monopile giving values equal to the unit. The model takes the average displacement and rotation at each node based on the force and the moment as equivalent. In order to avoid the reflections outside the domain of interest and achieve the radiation condition, Perfectly Matched Layers (PMLs) are added at the boundaries of the domain [6]. The degrees of freedom of the full model are condensed into the degrees of freedom at the boundary with the pile. It should be also mentioned that the model approaches the problem linearly and takes also into account the assumption that there is no fluid above the mud line, which is not totally in accordance with the present project.

However, it is considered acceptable, due to the absence of another method for reliable estimation of the soil coefficients.

The main idea of the model is that by applying the unit force and moment at each node, the flexibility matrix is obtained. Implementing the inverse of it, the dynamic stiffness matrix $\tilde{K}(\omega)$ is estimated for a specific frequency.

The properties of the soil profile are accounted for the derivation of the soil and damping coefficients. For the specific case, an homogeneous, half-infinite soil is considered, in order to capture the phenomenon of the radiation damping. As the geology in Taiwan is rather complex for the derivation of reliable information, the soil type was assumed as "medium dense sand" with the following average properties:

Young Modulus: $E=30 \text{ MPa}$

Poisson ratio: $\nu = 0.3$

Soil density: $\rho = 2000 \text{ kg/m}^3$

By including the specific model, the dynamic stiffness matrix is added to the solution of the dynamic problem, contributing to the derivation of the soil coefficients for every excitation frequency.

4.4. Formulation of Damping Matrix

The composition of the global damping matrix is of great interest, as the different sources of the damping were investigated and included as part of the total matrix. The present project focuses on the hydrodynamic and earthquake loads, and for that reason the study of the damping sources was based on the energy dissipation given to the system mainly because of these two loads.

Initially, it is stated that the assumption that the turbine is in non-operational state and the aerodynamic damping does not contribute to the dissipation of the energy of the system is made. This mainly holds because load cases with the application of aerodynamic loads are not part of the scope of the thesis. Additionally, the aerodynamic damping has the largest contribution to the total amount of damping when the turbine is in production state [22], and the effect of the other sources of damping is more easily clarified by not including that. Additional dampers are also not included in the system, therefore only the structural, the hydrodynamic and the soil damping are regarded.

For the representation of the structural damping, the Rayleigh Method [7] was used according to the mass and the stiffness proportionality. The damping ratio was selected equal to 1%, in agreement with the literature [22]. The derivation of the hydrodynamic damping is explained extensively in 4.4.1. The soil radiation damping is included through the dynamic stiffness matrix, as it is presented on Section 4.3.

The total Damping matrix [C] is composed considering all the previously mentioned amounts of damping sources, which are applied in the specific elements of the structure where each of them act. It should be highlighted that the resulted matrix is non-diagonal.

4.4.1. Hydrodynamic Viscous Damping

As it was described before, the hydrodynamic damping is the sum of the viscous and the radiation hydrodynamic damping. The radiation damping is not examined in the present study and for that reason it is assumed that it does not contribute to the total hydrodynamic damping. The viscous damping is expressed with the drag coefficient C_D and consequently, with the drag term of the Morison Equation.

Initially, the drag coefficient is calculated based on the equations of DNVGL-RP-C205 [10], presented on Chapter 2, highlighting the differences in each element of the structure under the wave action.

The chosen material for the whole structure is painted steel ($k = 5 * 10^{-6}$), resulting in the smooth case of Equation 2.12 and the same dependency of the drag coefficient on the surface roughness for all the elements.

Additionally, the KC number is derived for the elements under the hydrodynamic loads, by choosing the maximum particle velocity for each of them according to their water depth. Afterwards, the wake amplification factor was estimated from Equation 4.4.

Accounting for supercritical Reynolds numbers, the resulting drag coefficient for each element is estimated dependent on the surface roughness, the KC number and the Reynolds number, using Equation 2.13.

With this approach, the C_D coefficient becomes different for every element of the structure where the hydrodynamic loads act, depending also on the water depth and the diameter of every element. Hence, the viscous hydrodynamic force for the elements changes as well, based on the variations of the drag coefficient.

However, it should be noticed that the drag force of the Morison equation is non-linear (Equation 4.1), because of the squared velocity, and it does not result in the usual form of the damping force which should be proportional to the velocity. Additionally, it could not be used in the frequency domain because of the non-linearity. This fact makes the derivation of a hydrodynamic viscous coefficient more complicated.

The drag term of the Morison equation is equal to:

$$f_D = \frac{1}{2} C_D \rho D |u| u \quad (4.1)$$

In order to extract a specific viscous hydrodynamic damping coefficient that could be given for the elements under the action of hydrodynamic loads, and therefore to be used in order to formulate the damping

matrix, the non-linear drag force should be transformed in the form of the damping force (C^*u). To achieve this, the idea of the linearization of the drag force was emerged.

Borgman [23] proposed the linearization of the wave drag force using the random Gaussian process assumption for the wave velocity under the action of unidirectional wave, without current [14], concluding in:

$$f_D = \frac{1}{2} C_D \rho D \sqrt{\frac{8}{\pi}} \sigma_u u \quad (4.2)$$

There is also a concluded formula for multi-directional flow [14], although the aim of the present study is to estimate the amount of the viscous damping for the lateral loads in the x-direction, and for that reason this simplified case is applied. The drag force follows the form of the proportionality with the velocity, and the part $\frac{1}{2} C_D \rho D \sqrt{\frac{8}{\pi}} \sigma_u$ is considered as the viscous damping coefficient.

As the goal is to discretize the damping for the different elements, the assumption that the wave velocity is a random Gaussian process was tested for all the elements under the wave loads, in order to verify that the linearized form of the drag force could be applied. Afterwards, the standard deviation was calculated separately for each of the previous elements. Considering that the C_D coefficient and the diameter D differ for the elements, a separate hydrodynamic viscous damping coefficient is estimated for them, which is consequently added to the damping matrix only for these specific elements.

It should be noted that the linearization of the drag coefficient was applied separately of the estimation of the Morison equation, only regarding the derivation of the hydrodynamic viscous damping.

In the following Figures 4.3 to 4.9, the variation of the relative parameters across the length of the monopile is presented, resulting in the derivation of the drag coefficient and the hydrodynamic viscous damping coefficient. The accounted load case is for irregular waves with $H_s = 5m$ and $T_p = 6sec$. It should be noted that the specific case is shown as an example to highlight the dependency of the hydrodynamic viscous damping on the various parameters, although the same approach was followed for all the tested load cases of this thesis and had shown the same behaviour.

Initially, in Figure 4.3 the change of the diameter along the interested part of the structure is presented, which plays an important role for the estimation of the drag coefficient, as it is accounted in all the relevant parameters, such as KC and C_{DS} .

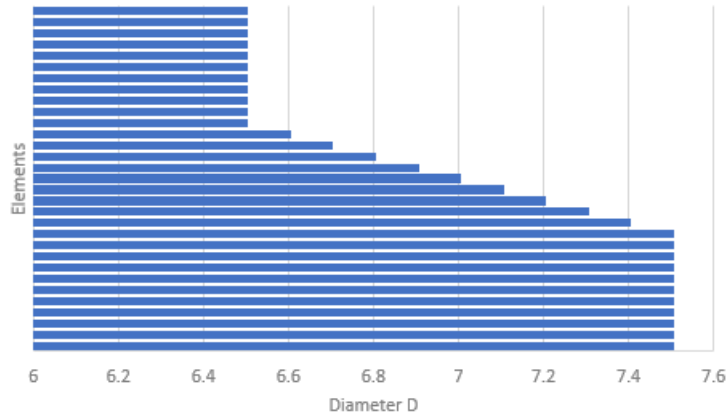


Figure 4.3: Variation of the diameter along the length of the monopile

The estimation of the C_{DS} coefficient, which shows the relationship between the drag coefficient and the surface roughness, is not depicted, as by choosing the painted steel for all the elements, it does not have any difference along the length of the structure.

The next crucial step is the derivation of the KC number. As the KC number is proportional to the maximum orbital velocity, it is observed in Figure 4.4 that it follows the exponential behaviour of the velocity profile [13].

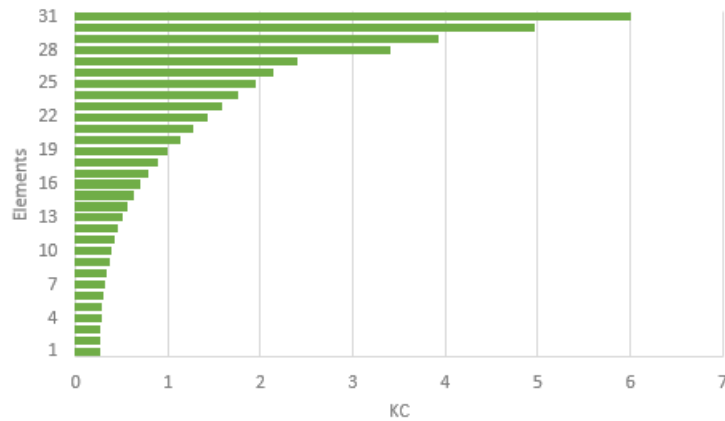


Figure 4.4: Variation of the KC number along the length of the monopile

Afterwards, the wake amplification factor is presented in Figure 4.5, which is a function of the KC number. However, it does not follow the same behaviour as the KC number, because as it is apparent from Equation 2.14, its calculation varies according to the value of the KC number.

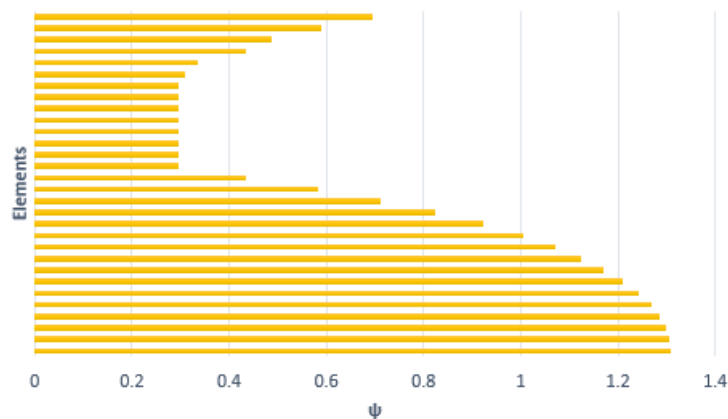


Figure 4.5: Variation of the wake amplification factor along the length of the monopile

Based on Equation 2.13, the resulting drag coefficient is derived. It is concluded from Figure 4.6, that is obviously dependent on the wake amplification factor, and respectively on the KC number, showing the same form along the length of the monopile. This is reasonable, as the dependency on the surface roughness is relatively low. The drag coefficient has the maximum value at the lowest element, which is in the mud line.

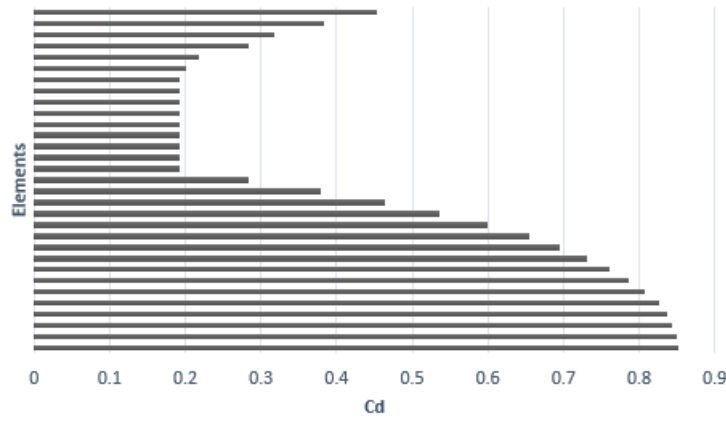


Figure 4.6: Variation of the drag coefficient along the length of the monopile

For the derivation of the hydrodynamic viscous damping coefficient the standard deviation of the velocities for each element were also estimated, as it is presented in Figure 4.7.

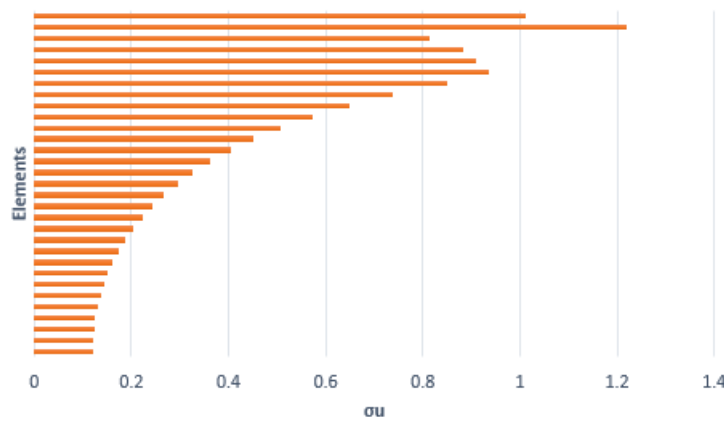


Figure 4.7: Variation of the standard deviation of the velocity along the length of the monopile

In Figure 4.8, the variation of the resulting hydrodynamic viscous damping coefficient is shown, which generally has higher values at larger depths than the mud line. It does not follow a specific behaviour because it is also dependent on the diameter and the drag coefficient, which have larger values closer to the mud line.

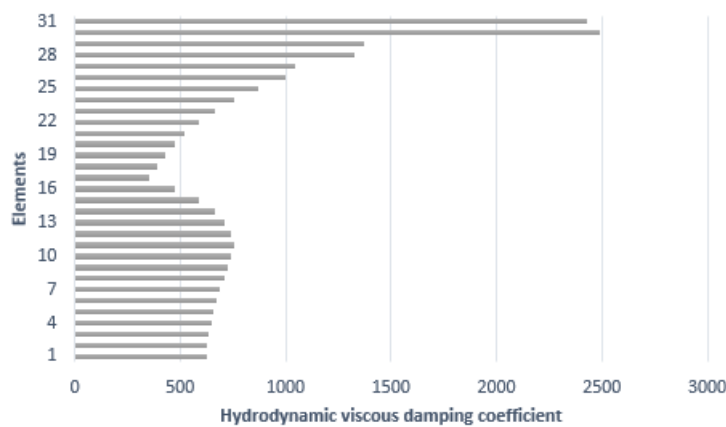


Figure 4.8: Variation of the hydrodynamic damping coefficient of the velocity along the length of the monopile

In Figure 4.9, the wave amplification factor is shown as a function of the KC number and the C_{DS} coefficient for the specific case, as it is also presented on Figure 2.1 according to DNV-RP-C205 [10]. It is observed that that it has the same form as it was expected for low KC numbers and the smooth case of the surface roughness.

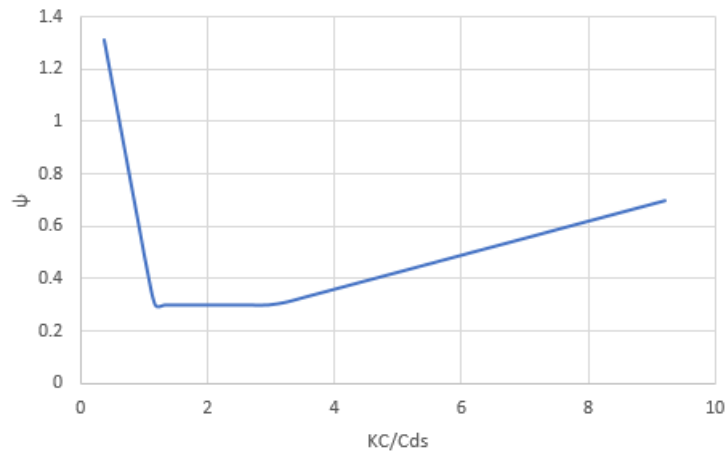


Figure 4.9: Wake amplification factor ψ as a function of KC number for $C_{ds} = 0.65$

The values for the derivation of the presented Figures, are shown analytically on the Appendix B.

4.5. Loads

In the present research, it is assumed that only lateral loads act on the structure, with main interest on the hydrodynamic and earthquake loads. The aerodynamic loads are not included in the load cases.

In this Section, the implementation of the lateral loads formulating the total Force Matrix is described.

4.5.1. Hydrodynamic loads

The Python Design Tool accepts as input the type of the wave spectrum and main properties, such as the wave period and the significant wave height. The model accepts as input both JONSWAP and Pierson-Moskowitz wave spectra for developing and fully developed sea states, respectively. Based on the information of the spectrum, the corresponding wave theory (Airy wave theory, Stokes theory) is used to determine the wave particle hydrodynamics until the mean sea level, and then the Wheeler Stretching Method for the extrapolation of the total wave elevation.

For the estimation of the hydrodynamic loads, the Morison equation is used. As it is known, the Morison equation consists of two parts, the inertia and the drag part. The former part is proportional to the particle acceleration and the later part is proportional to the particle velocity.

$$F = \frac{1}{4} C_M \rho \pi D^2 a + \frac{1}{2} C_D \rho D |u| u \quad (4.3)$$

The drag term leads to the hydrodynamic viscous damping and as it was mentioned before it is expressed with the drag coefficient C_D . It is common to select a constant value for the drag coefficient along the length of the structure. In the specific study, instead of taking a constant value for C_D , the dependence of it on the Reynolds number, the surface roughness and the KC number was highlighted based on the equations proposed by DNV-RP-C205 [10] for oscillatory flow. This procedure is followed for every element along the length of the structure where the wave loads act, taking also into consideration the differences in the diameter and the water depth. The wave forces for each part of the structure are then computed and added to the Force Matrix.

For the followed approach of the linearization of the drag term that was applied to the hydrodynamic viscous coefficient, a main assumption was that currents should not be present [14]. For that reason, currents are not included as part of the hydrodynamic loads in the present study.

4.5.2. Earthquake loads

The estimation of the earthquake loads is based on the response spectrum method [12]. As the possibility of using data based on real earthquake is limited, artificial response spectra are used as input to the model, which are created according to the procedure presented in Figure 4.10. The response spectrum is considered as a series of maximum time history responses of one-degree-of freedom systems having different natural frequencies [21].

The acceleration time signal is constructed as it is shown in Equation 4.4.

$$\ddot{u}_g = \sum_{n=1}^N S_n \sin(\omega_n t + \phi_n) \quad (4.4)$$

where:

S_n is the magnitude of the response spectrum n ,

ω_n is the natural frequency of the response spectrum n

ϕ is the random time shift.

The total earthquake force are calculated as $M * A(\ddot{u}_g)$, where M is the Mass Matrix and A is the amplification factor that increases the based acceleration depending on the soil layer characteristics.

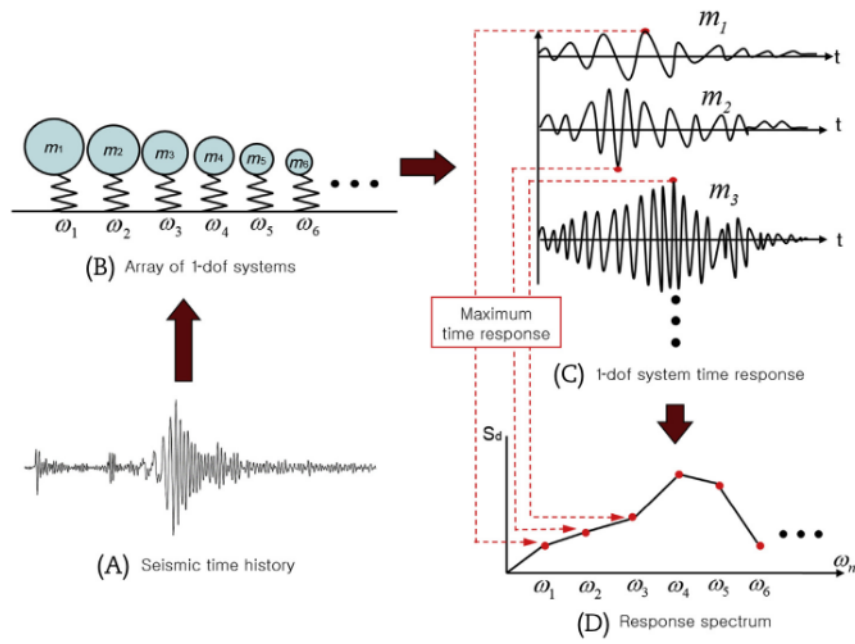


Figure 4.10: Concept of the Response Spectrum

It should be mentioned that the earthquake force is applied on every node of the structure below the mud line. However, it does not consider the change regarding the depth, which could be a valuable step for further improvement of the application of earthquake loads in the model.

4.6. Solution of the Dynamic Problem

The equation of motion for the total structural system has the general form of a damped system subjected to harmonic forces. The equation is presented in the form of coupled matrices for M , C , K and F :

$$M\ddot{x} + C\dot{x} + Kx = F \quad (4.5)$$

Where: x is the displacement, \dot{x} is the velocity and \ddot{x} the acceleration of the system.

However, if the soil and damping coefficients are going to be included in the previous equation, the system cannot be solved in the time domain. This happens because of the fact that the coefficients are based on the dynamic impedance functions, which are frequency-dependent. Hence, the system should be solved in the frequency domain.

Initially, the general solution should be transferred in the frequency domain. This can be accomplished by making use of the Fourier Transform:

$$x(t) = \frac{1}{2\pi} \int_{-\infty}^{+\infty} \tilde{x}(\omega) \exp(i\omega t) d\omega \quad (4.6)$$

The Force matrix is also calculated in the time domain and it has also to be transferred in the frequency domain by FFT.

Substituting these to Equation 4.5, results in the following:

$$(-\omega^2 M + i\omega C + K)\tilde{x}(\omega) = F(\omega) \quad (4.7)$$

The dynamic impedance function can be presented separately in the equation of motion in the frequency domain:

$$(-\omega^2 M + i\omega C + K + \tilde{K}(\omega))\tilde{x}(\omega) = F(\omega) \quad (4.8)$$

Where:

$$\tilde{K}(\omega) = \hat{K}(\omega) + i\omega\tilde{C}(\omega) \quad (4.9)$$

The dynamic impedance function is estimated for the part of the structure below the mud line, as it was explained previously, for every excitation of interest.

The method that is widely used in order to solve the dynamic problem with many DoFs in the time domain, is the classical modal analysis. It transforms the equations of motion in modal coordinates so as to uncouple them, and depending on the number of the modes computed, it reduces the size of the problem. For that reason, it can be adopted more easily for large systems. The modal response of the structure can also be applied in the frequency domain.

Nonetheless, the modal analysis can be applied only in cases where no or modal damping is present. This is not valid for the present study, as the inclusion of the dynamic impedance function assembles the matrix non-diagonal.

Additionally, a crucial step for the modal analysis is the estimation of the natural frequencies and the modes through the solution of the eigenvalue problem. For non-classically damped systems, the complex eigenvalue problem should be solved [25]. However, as the stiffness and the damping matrices depend also in the frequency ω , the estimation of the natural frequencies and the modes becomes more complicated.

In order to avoid possible errors for the previous mentioned reasons, the direct analysis in the frequency domain was chosen for the solution of the dynamic problem. It is not so computationally efficient, but it is more accurate as it is not based on the estimation of the modes. In the direct analysis, the coupled form of the equation of motion (Eq. 4.8) is solved at discrete frequencies using complex algebra.

More specifically, the equation 4.8 is turned to the form:

$$\tilde{x}(\omega) = \frac{1}{(-\omega^2 M + i\omega C + K + \tilde{K}(\omega))} F(\omega) \quad (4.10)$$

Where:

$$H(\omega) = \frac{1}{(-\omega^2 M + i\omega C + K + \tilde{K}(\omega))} \quad (4.11)$$

Or:

$$\tilde{x}(\omega) = H(\omega) * F(\omega) \quad (4.12)$$

The function $H(\omega)$ is known as *complex frequency-response or transfer function*. The product of the response function and the force in the frequency domain, gives the steady-state response $\tilde{x}(\omega)$, as it can be seen in equation 4.10.

The steady-state response of the structure $\tilde{x}(\omega)$ is then estimated for the range of the forcing frequencies. The decision of the band of the frequencies depends on the discretization of the applied forces during the total time interval that they act on the structure. More specifically, the selected range of the frequencies is the same as the frequencies in which the Fourier transform is applied to the forces, which as it is known, depend on the total duration of the forces and the sampling interval used to separate them into samples.

For the estimation of the response of the structure in the time domain, the inverse Fast Fourier Transform is applied to the results based on Equation 4.10. However, it is important to state that as the response in the frequency domain gives only the steady-state response, with the implementation of the inverse Fourier Transform the result represents again the steady-state response in time domain. The resulting response may deviate from the actual transient response [4].

4.7. Eigenvalue Problem

As it was discussed, the solution of the eigenvalue problem for a non-classically frequency-dependent damped system is complicated, hence it was preferred to continue with the direct frequency analysis to avoid possible errors. However, in order to have a general outcome about the approximate values of the natural frequencies, the eigenvalue problem was estimated for the static case, accounting the values for the soil stiffness and damping only for the zero frequency.

The first five natural frequencies are the following:

$$\left| \begin{array}{l} f_1 = 0.217Hz \\ f_2 = 1.524Hz \\ f_3 = 3.936Hz \\ f_4 = 5.891Hz \\ f_5 = 7.774Hz \end{array} \right|$$

Table 4.1: Approximate Values of the Natural Frequencies

The estimation of the natural frequencies for the simplified case gives a general benefit for the comprehension of the results in the frequency domain.

4.8. Validation of the solution of the model in the Frequency domain

For the verification of the results given from the solution of the dynamic problem with the direct frequency analysis, a simplified case was tested where the monopile was totally constrained to its base without accounting the soil-structure interaction, as shown in Figure 4.11. The response of the structure estimated from the direct frequency analysis and transformed back to the time domain using Inverse Fast Fourier Transform (IFFT), was compared with the one calculated from a direct time-domain analysis (Figure 4.12), which was already developed on the Python Design Tool. The tested load case accounts only regular waves ($H_s = 5m$, $T_p = 5sec$) acting on the structure. The hydrodynamic damping and the Rayleigh damping with damping ratio 2% were considered in both cases for the dissipation of energy.

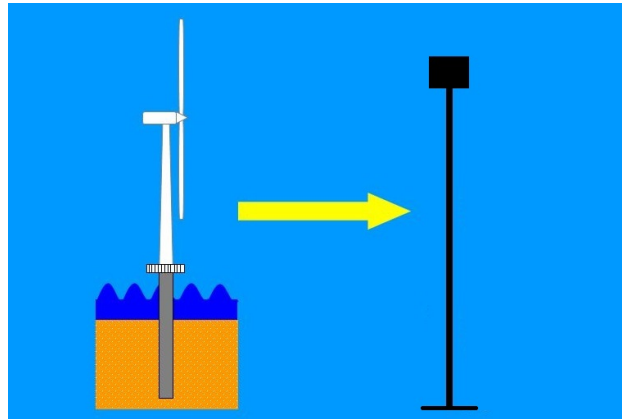


Figure 4.11: Fixed-bottom monopile

In Figure 4.12, the response of the structure of the node at the top of the tower is shown for a time span of 1400 sec. It is observed that the steady-state response is reached after the 600 sec.

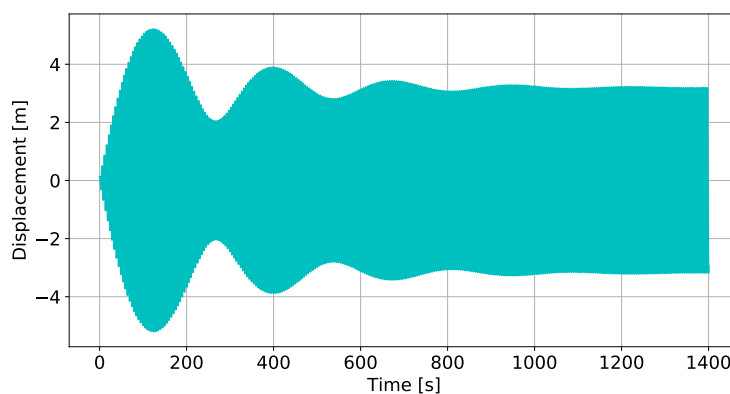


Figure 4.12: Direct Time Domain Analysis

In Figure 4.13, the response of the structure of the node at the top of the tower is depicted, which was derived through the direct frequency analysis and the Inverse Fourier Transform for 100 sec.

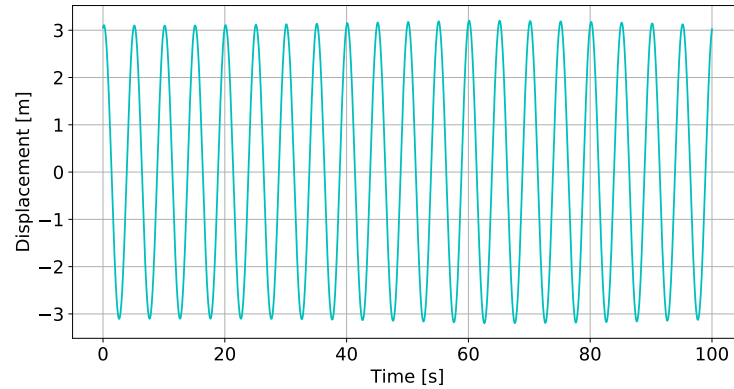


Figure 4.13: Direct Frequency Domain Analysis

Comparing Figures 4.12 and 4.13, it is verified that the direct frequency analysis gives directly the steady-state response of the structure at the first 100 sec neglecting the initial transient part. The amplitudes of the displacement are also in accordance in the two cases (approximately $2.8m$), leading to the conclusion that the result of the Inverse Fourier Transform for the response of the structure from the direct frequency analysis does not lead to significant errors in the results.

Afterwards, the complete model including the soil-structure interaction was included, as it is depicted in Figure 4.14. Comparing it with Figure 4.13, it is verified that the involvement of the SSI decreases the response of the structure. The maximum amplitude in Figure 4.13 is around $3.2m$, while in Figure 4.14 the highest reached value is about $0.28m$.

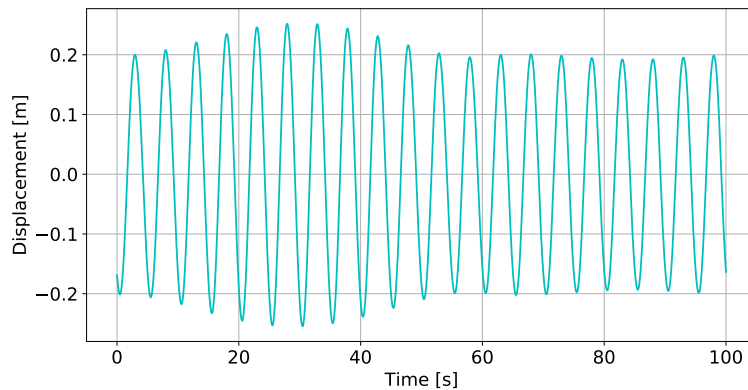


Figure 4.14: Soil-structure Interaction Included

Figure 4.15 shows the results of the response of the structure, where the dynamic stiffness matrix and the hydrodynamic damping are included, without the Rayleigh damping representing the structural damping. In comparison with the Figure 4.14, it is concluded that the two Figures are identical and the Rayleigh damping has not effect on the response of the structure during the presence of the SSI.

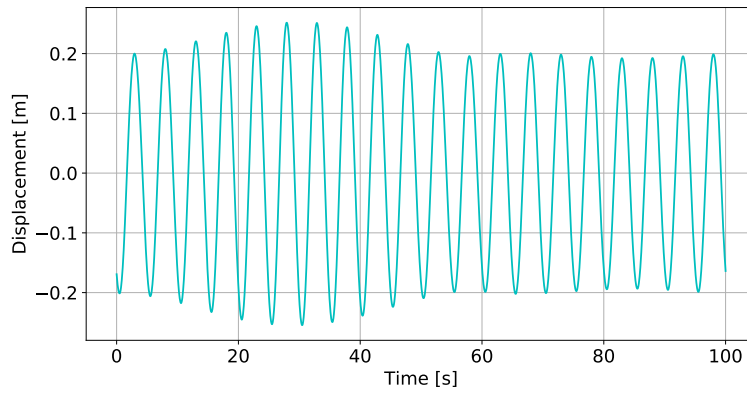


Figure 4.15: Rayleigh damping Included

The Rayleigh damping is not added as part of the total damping matrix for the rest of the study, because, as it was stated before, it is not preferable for the solution of the problem with the direct frequency analysis.

5

Results & Discussion

In this chapter the dynamic analysis of the response of the structure is presented, examining load cases with hydrodynamic and earthquake loads in order to investigate the consequences of the hydrodynamic viscous and soil radiation damping to an offshore wind turbine structure. The response of the structure is shown in both time and frequency domains.

The applied load cases are the following:

- Hydrodynamic loads (Irregular waves)
- Hydrodynamic (Regular waves) & Earthquake loads
- Hydrodynamic (Irregular waves) & Earthquake loads

As it is mentioned in Chapter 4, for the application of the earthquake loads the Response spectrum method is used, with the following spectrum given as input for the model for all the cases.

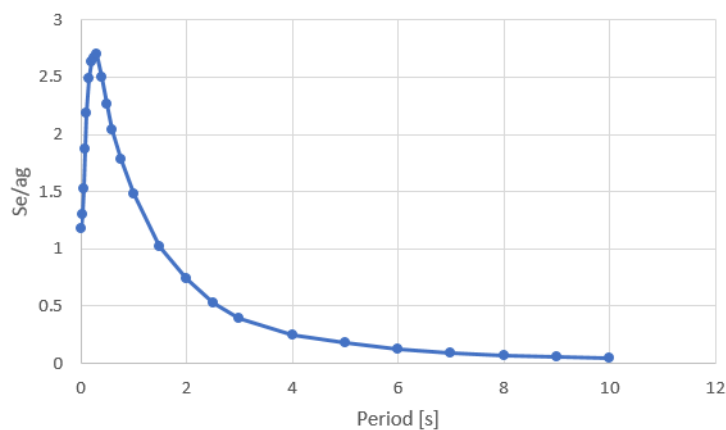


Figure 5.1: Response spectrum of the earthquake

For the hydrodynamic loads, the details of the input wave spectrum are referred in each case separately.

In these three load cases, the presence of the hydrodynamic viscous damping is tested. Additionally, in order to highlight the effect of the frequency-dependent dynamic soil matrix, the comparison with the static

case is presented, where only the values of the soil stiffness and damping coefficients for frequency equal to zero are considered without changing for every forced frequency.

For the analysis of the structural response in the frequency domain for the considered cases, the Figures for the amplitude spectrum are presented as single-sided, only for the positive frequencies based on the Nyquist theorem [1]. Moreover, the spectrum is scaled by multiplying with $2/N$, in order to get the correct amplitude for the frequencies.

The Power density spectrum is also derived for the tested cases, which shows the distribution of the power into the different frequency components [2]. The Power Spectral Density is a useful method to check the natural frequencies of the structure, as well as the damping [9]. The PSD is derived as the absolute squared value of the amplitude response values.

The response is studied for critical points of the structure, such at the top of the tower and the mud line.

5.1. Dynamic Impedance Function

The dynamic impedance function $\tilde{K}(\omega) = \hat{K}(\omega) + i\omega\tilde{C}(\omega)$ should be approximated based on the excitation frequencies ω of the applied load cases. This means that the range of the frequencies is affected by the total time interval and the time step that the forces are applied on the structure.

For the three tested load cases, the total time interval that the forces were acting on the structure was the same (100 sec), because as the dynamic problem is solved for every frequency, the derivation of the dynamic stiffness matrix requires high computational time.

The coefficients of the dynamic stiffness matrix were estimated for every node of the structure below the mud line. However, in the following Figures only the values for the point at the mud line and the monopile tip are presented considering the horizontal and rotational motion.

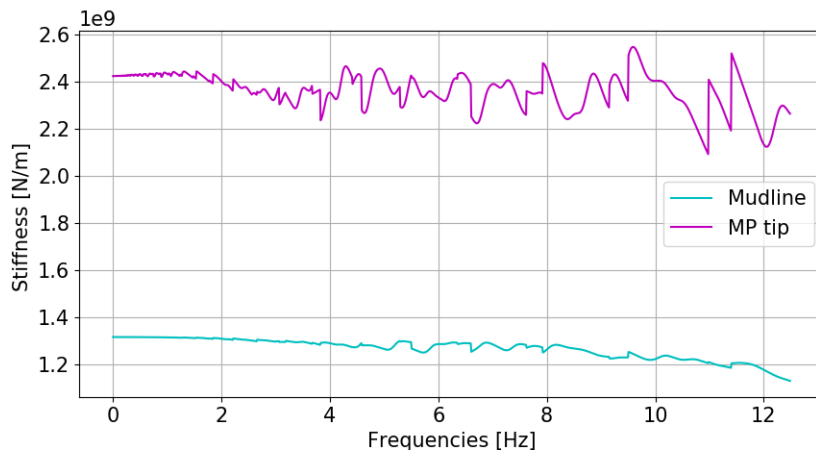


Figure 5.2: Soil Stiffness as a function of frequency for horizontal translational motion

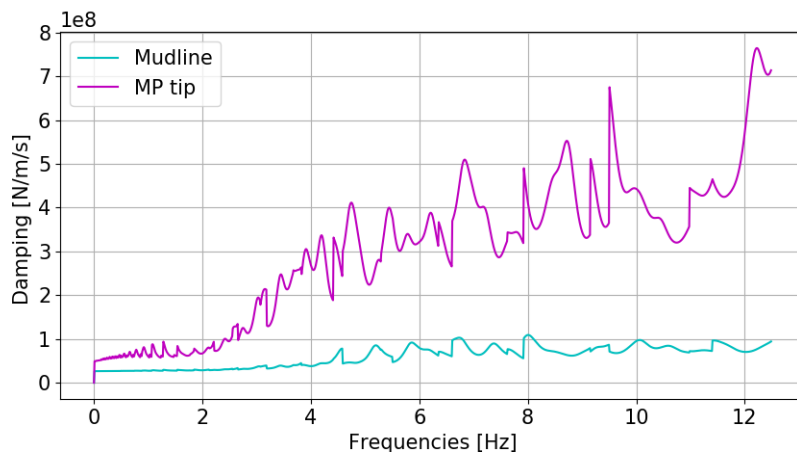


Figure 5.3: Soil damping as a function of frequency for horizontal translational motion

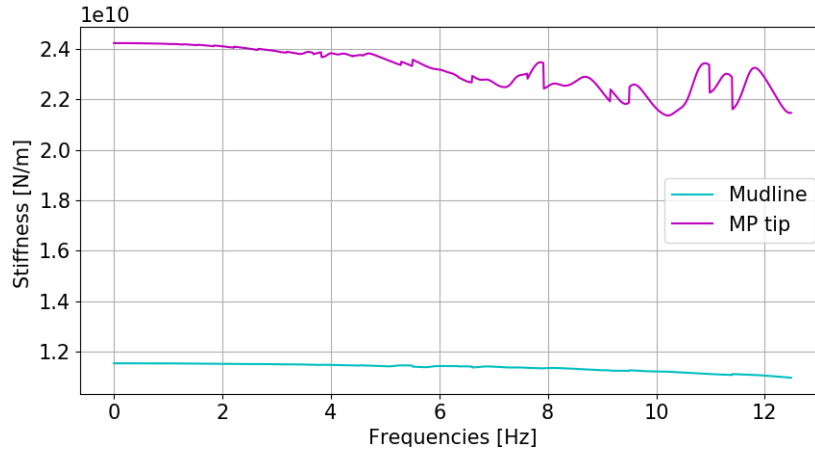


Figure 5.4: Soil Stiffness as a function of frequency for rotational motion

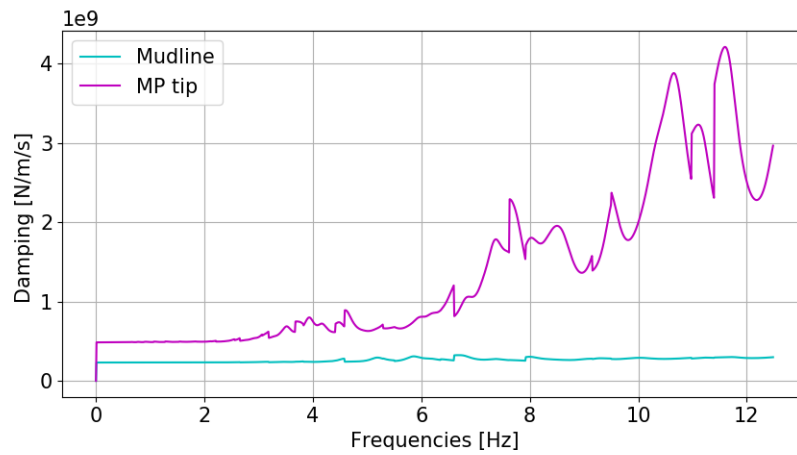


Figure 5.5: Soil damping as a function of frequency for rotational motion

In Figures 5.2 and 5.4, the real part of the dynamic impedance function is shown for the horizontal and the rotational motion. In Figures 5.3 and 5.5, the imaginary part for the horizontal and rotational motion is illustrated.

Generally, it is observed that the Figures follow the form that was expected based on the literature (Figure 3.2). However, as the frequency step was selected based on the excitation frequencies and it is not an integer number, their form is not smooth. The used soil model gives better estimations for integer and larger frequency steps than the applied one in the specific cases.

It should be also mentioned that in the monopile tip, the stiffness and the damping have higher values than in the mud line, showing that the dynamic stiffness matrix is also dependent on the depth.

5.2. Hydrodynamic Loading

A first approach of the problem is the application of hydrodynamic loads on the structure, without the presence of earthquake, considering irregular waves acting on the structure with $H_s = 5m$, $T_p = 6sec$.

Initially, for the solution of the problem, only the hydrodynamic damping and the static case for the dynamic stiffness were considered, as it is portrayed in Figures 5.6 to 5.14 for the points at the top of the tower, at the mud line and at the height $+2.00m$ LAT. The last point was selected because, as it was concluded in Chapter 4, in this height the hydrodynamic viscous damping has the largest contribution.

Generally, it is stated that the displacements of the structure are rather small for this specific case, as it is observed in Figures 5.6 and 5.9. This happens because of the inclusion of the soil-structure interaction in the model. For the analysis in the frequency domain, it is seen in the amplitude and PSD spectra that peaks arise in the natural frequencies estimated for the static case (Chapter 4). Moreover, Figures 5.7 and 5.8 are presented only for lower frequencies, because their values are close to zero for higher frequencies. The amount of damping that is present during a case can be estimated based on the half-power bandwidth method [17]. The process is based on the diagram of the Power Spectral Density, where the frequency f_n is observed with the maximum power P_{max} , the frequencies f_1 and f_2 with power $P_{max}/2$ and the value of the damping is given by Equation 5.1.

$$2\zeta = \frac{f_2 - f_1}{f_n} \quad (5.1)$$

In Figure 5.8, a peak is observed in the first natural frequency around 0.218 Hz, where the largest amount of energy is concentrated. The damping ratio is estimated around 2.5%.

In Figures 5.15 to 5.20, the hydrodynamic damping is not included, and the only source of damping contributing to the system is because of the dynamic stiffness matrix, and more specifically the soil radiation damping. Comparing Figures 5.9 and 5.15, it is observed that there are slight differences in the amplitudes of the displacements at the mud line, as for example at $t = 56sec$. The same conclusion arises also from Figures 5.12 and 5.18. A comparison between the spectra shows that there is a decrease in the amplitude when the hydrodynamic damping is present. However, for the considered load case, the displacements are relatively low and the differences based on the hydrodynamic damping seem negligible. Moreover, the hydrodynamic damping does not seem to have a dependency on the frequency, as there is no variation in results for the frequencies.

Furthermore, it is examined how the total frequency-dependent dynamic impedance function affects the response of the structure to hydrodynamic loads, as it is depicted in Figures 5.21 to 5.23. A comparison between the displacements (Figures 5.9 & 5.21) show that by including the frequency-dependent SSI, the maximum amplitude is decreased by 50%.

The amplitude spectrum gives a better understanding of the effect of the frequency-dependency to the structural response, although the values are very low for the present case. Figure 5.22 shows that the radiation damping contributes more to higher frequencies, where the amplitudes are close to zero. Nonetheless, it does not dissipate the energy that is concentrated on the first peak of the spectrum, as it is depicted in Figure 5.23.

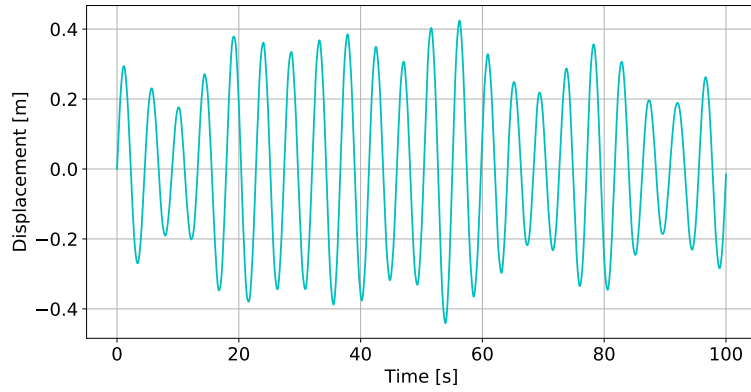


Figure 5.6: Displacement of node at the top of the tower under the action of irregular waves ($H_s = 5m$, $T_p = 6sec$) with the presence of hydrodynamic and static radiation damping

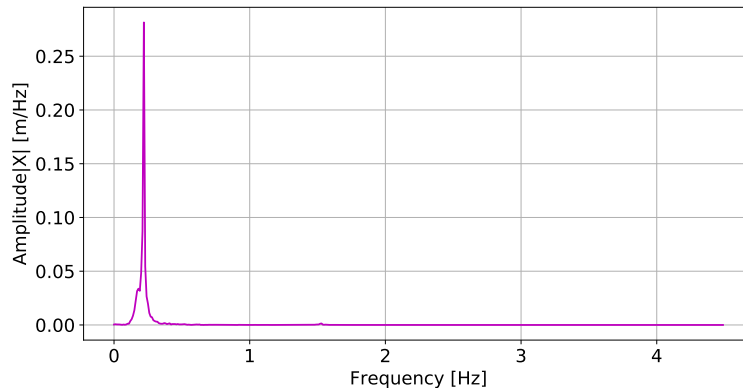


Figure 5.7: Amplitude spectrum of the node at the top of the tower under the action of irregular waves ($H_s = 5m$, $T_p = 6sec$) with the presence of hydrodynamic and static radiation damping

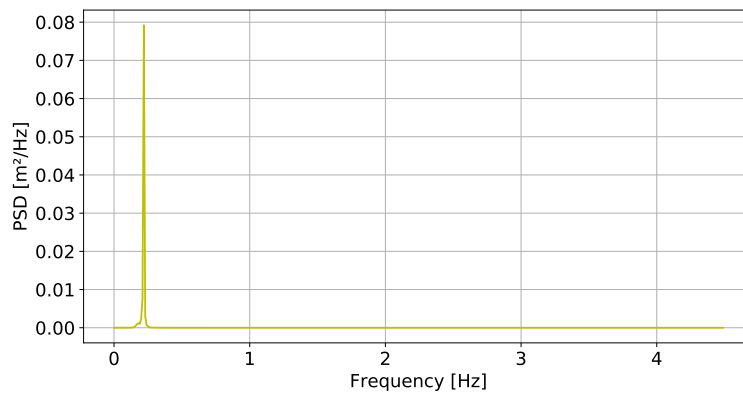


Figure 5.8: Power Spectral Density of the node at the top of the tower under the action of irregular waves ($H_s = 5m$, $T_p = 6sec$) with the presence of hydrodynamic and static radiation damping

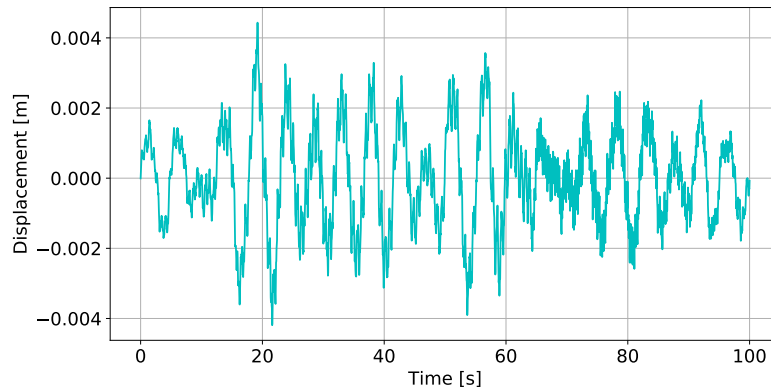


Figure 5.9: Displacement of the node at the mud line under the action of irregular waves ($H_s = 5m$, $T_p = 6sec$) with the presence of hydrodynamic and static radiation damping

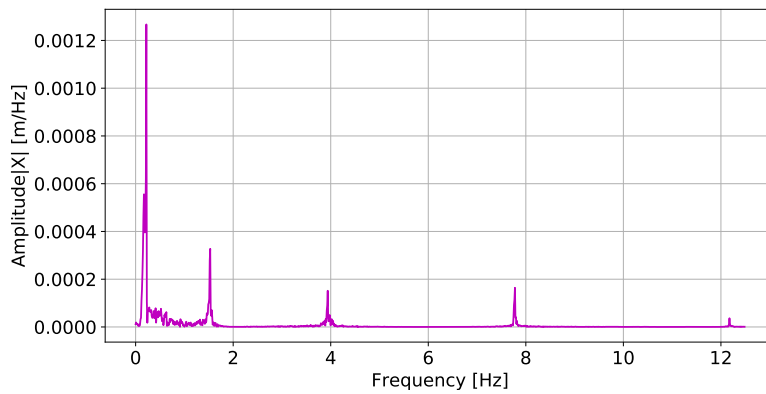


Figure 5.10: Amplitude spectrum of the node at the mud line under the action of irregular waves ($H_s = 5m$, $T_p = 6sec$) with the presence of hydrodynamic and static radiation damping

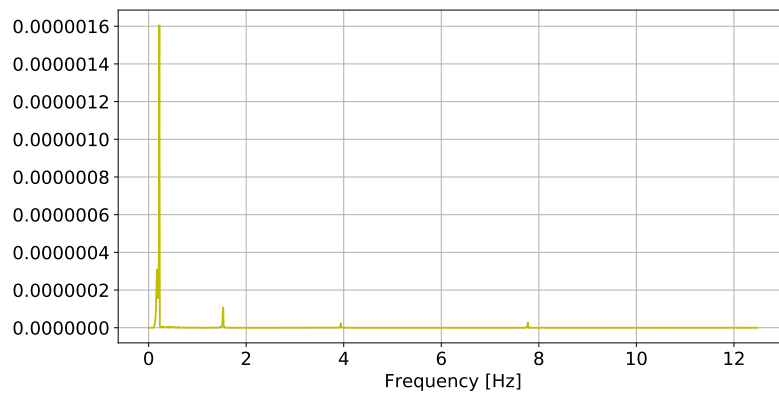


Figure 5.11: Power Spectral Density of the node at the mud line under the action of irregular waves ($H_s = 5m$, $T_p = 6sec$) with the presence of hydrodynamic and static radiation damping

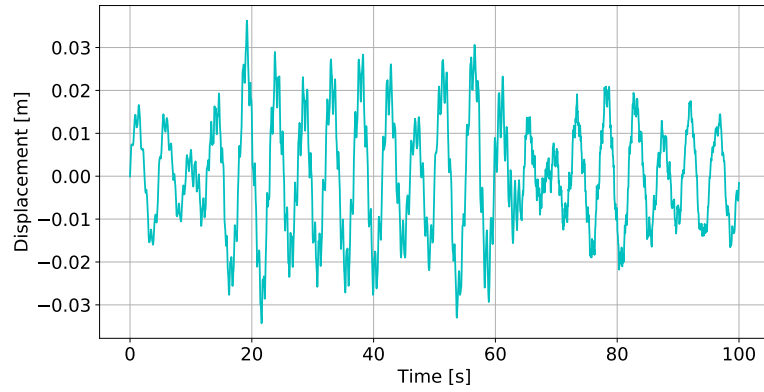


Figure 5.12: Displacement of the node at height +2.00m LAT under the action of irregular waves ($H_s = 5m$, $T_p = 6sec$) with the presence of hydrodynamic and static radiation damping

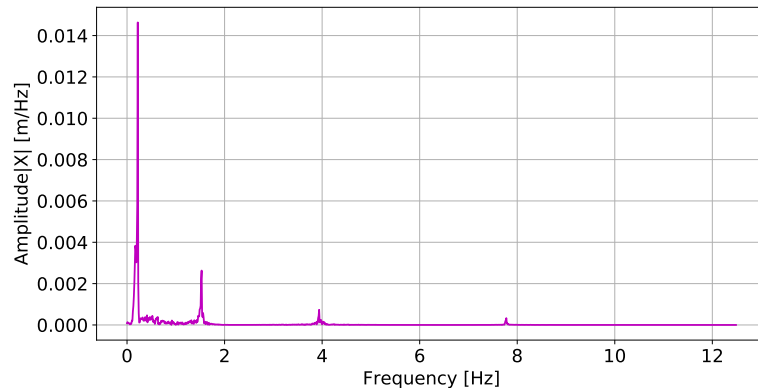


Figure 5.13: Amplitude spectrum of the node at height +2.00m LAT under the action of irregular waves ($H_s = 5m$, $T_p = 6sec$) with the presence of hydrodynamic and static radiation damping

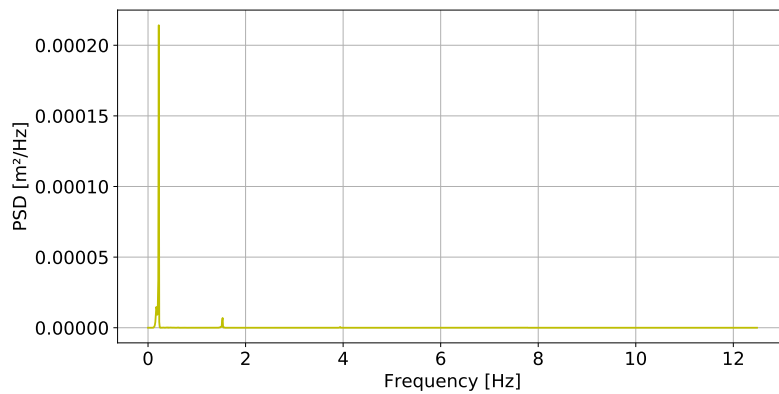


Figure 5.14: Power Spectral Density of the node at height +2.00m LAT under the action of irregular waves ($H_s = 5m$, $T_p = 6sec$) with the presence of hydrodynamic and static radiation damping

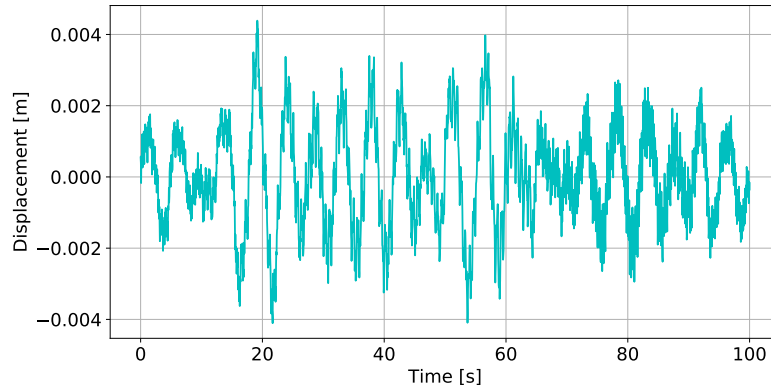


Figure 5.15: Displacement of the node at the mud line under the action of irregular waves ($H_s = 5m$, $T_p = 6sec$) with static radiation damping (hydrodynamic damping is not included)

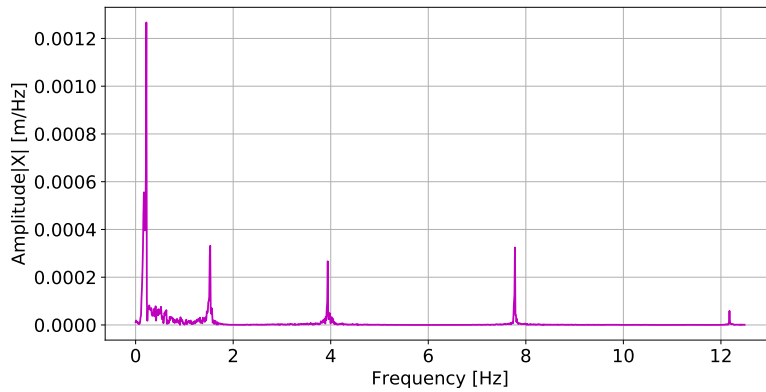


Figure 5.16: Amplitude spectrum of the node at the mud line under the action of irregular waves ($H_s = 5m$, $T_p = 6sec$) with static radiation damping (hydrodynamic damping is not included)

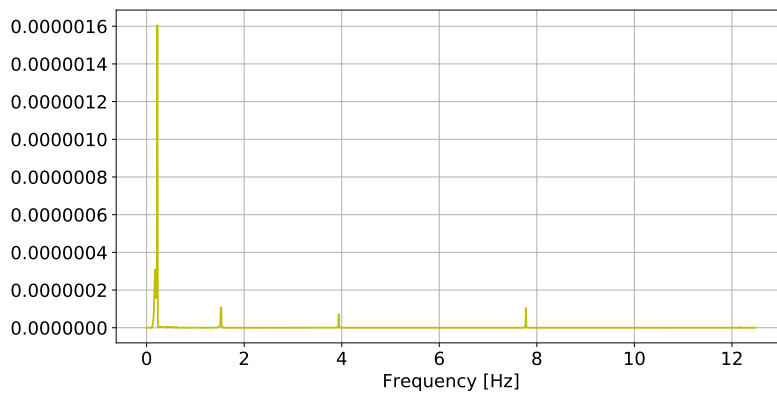


Figure 5.17: Power Spectral Density of the node at the mud line under the action of irregular waves ($H_s = 5m$, $T_p = 6sec$) with static radiation damping (hydrodynamic damping is not included)

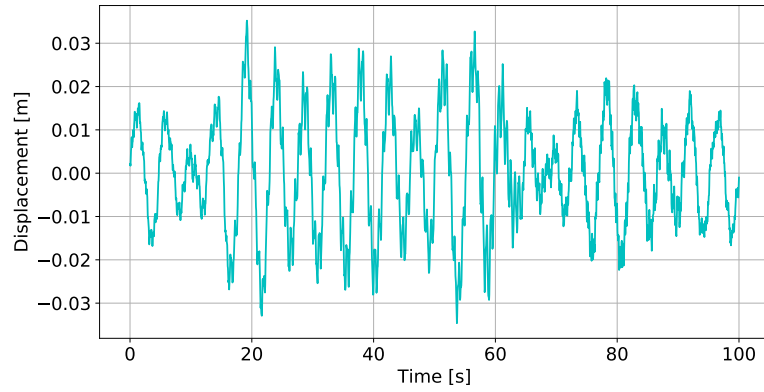


Figure 5.18: Displacement of the node at height +2.00m LAT under the action of irregular waves ($H_s = 5m$, $T_p = 6sec$) with static radiation damping (hydrodynamic damping is not included)

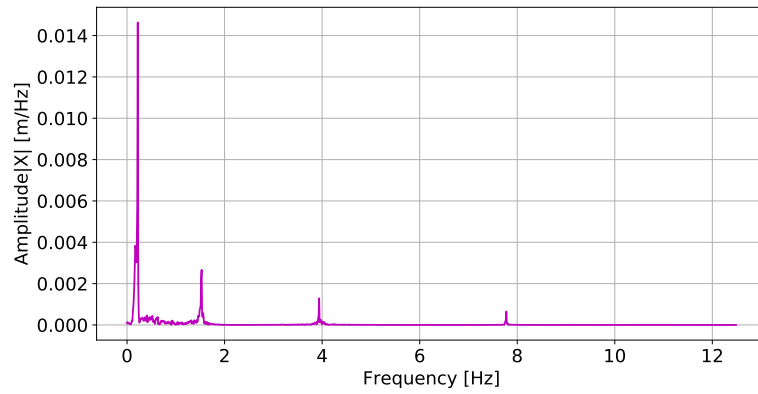


Figure 5.19: Amplitude spectrum of the node at height +2.00m LAT under the action of irregular waves ($H_s = 5m$, $T_p = 6sec$) with static radiation damping (hydrodynamic damping is not included)

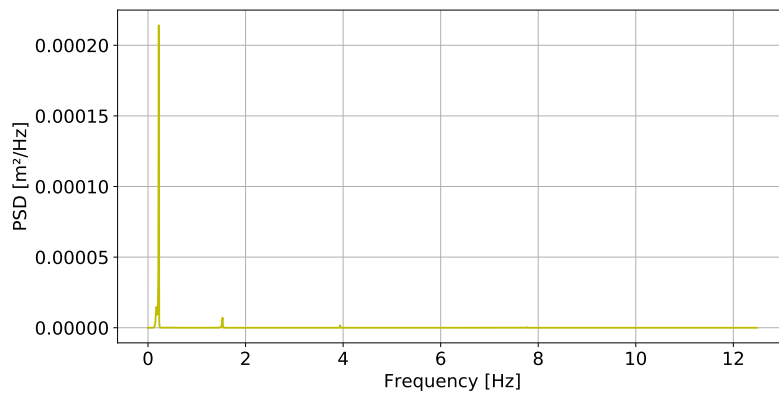


Figure 5.20: Power Spectral Density of the node at height +2.00m LAT under the action of irregular waves ($H_s = 5m$, $T_p = 6sec$) with static radiation damping (hydrodynamic damping is not included)

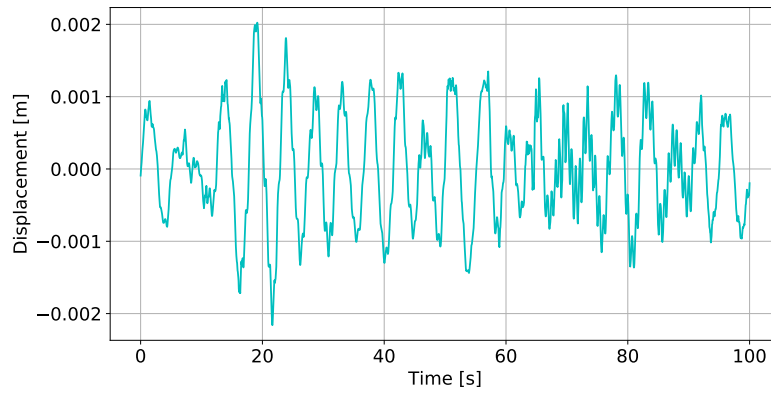


Figure 5.21: Displacement of the node at the mud line under the action of irregular waves ($H_s = 5m$, $T_p = 6sec$) with the presence of hydrodynamic and frequency-dependent radiation damping

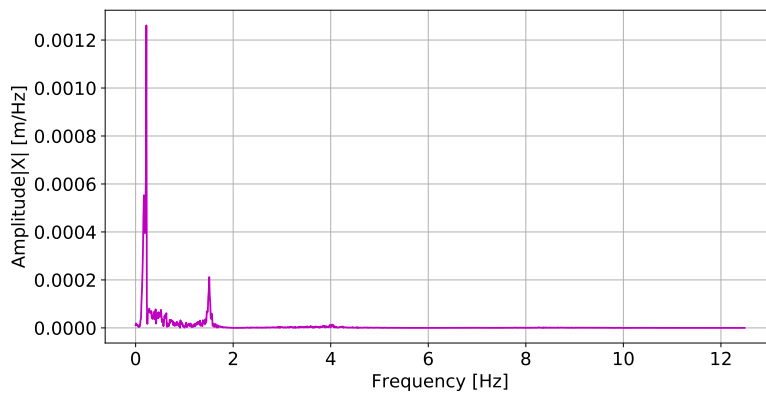


Figure 5.22: Amplitude spectrum of the node at the mud line under the action of irregular waves ($H_s = 5m$, $T_p = 6sec$) with the presence of hydrodynamic and frequency-dependent radiation damping

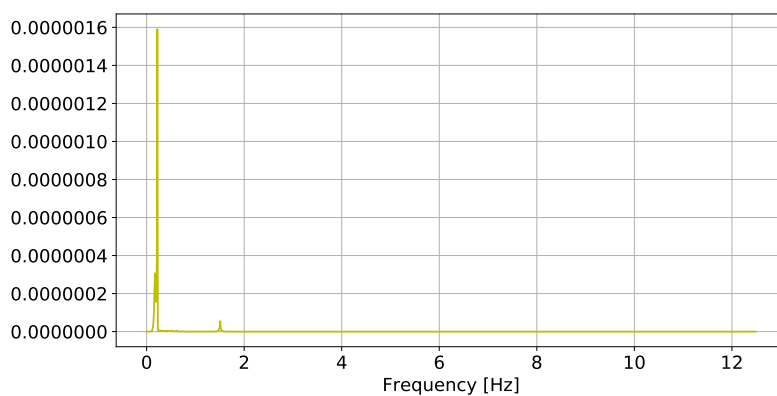


Figure 5.23: Power Spectral Density of the node at the mud line under the action of irregular waves ($H_s = 5m$, $T_p = 6sec$) with the presence of hydrodynamic and frequency-dependent radiation damping

5.3. Earthquake & Hydrodynamic Loading

5.3.1. Response to Earthquake & Regular Waves

A next step is the study of the structural response under the joint action of hydrodynamic and earthquake loads. In order to make the effect of the earthquake more evident, regular waves are applied with a low wave height ($H_s = 0.3m$, $T_p = 5sec$). For the present case, the accelerations of the interested points are presented, as it seems more meaningful for seismic loads.

The hydrodynamic damping is taken into account for this load case, although its contribution is very low. The static and the frequency-dependent cases are compared for the points at the top of the tower and at the mud line. A correlation between the acceleration at the tower (Figures 5.24 & 5.30) and at the mud line (Figures 5.27 & 5.33) show that the logarithmic form of the decrease is more intense when the frequency-dependent SSI is included. Moreover, the maximum values of the accelerations are lower in that case.

The spectra of the accelerations, especially at the mud line, show that multiple frequencies are excited at higher values, where the earthquake is present. However, when the frequency-dependent dynamic stiffness matrix is included, the amplitudes are decreased at these higher frequencies (Figure 5.34). This happens because the stiffness is decreased and the damping is increased in higher frequencies (Section 5.1).

The power spectra of the node at the top of the tower (5.29 & 5.32) show that there is power concentrated at the lower frequencies. In Figure 5.29, it is observed that there is a peak close to $8Hz$, which goes to zero (Figure 5.35), when the frequency-dependent SSI is accounted.

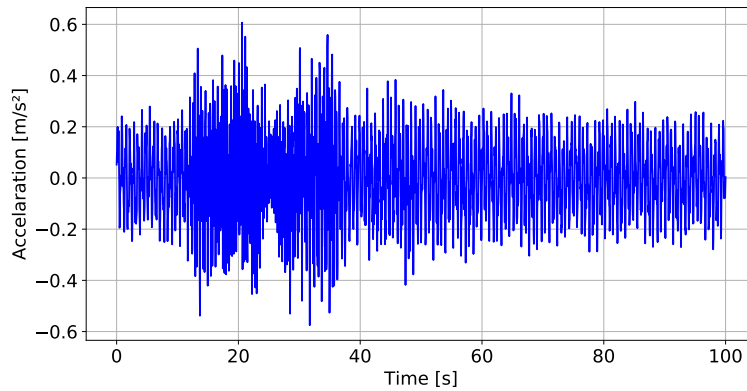


Figure 5.24: Acceleration of the node at the top of the tower under the action of regular waves ($H_s = 0.3m$, $T_p = 5sec$) & earthquake loads with the presence of hydrodynamic and static radiation damping

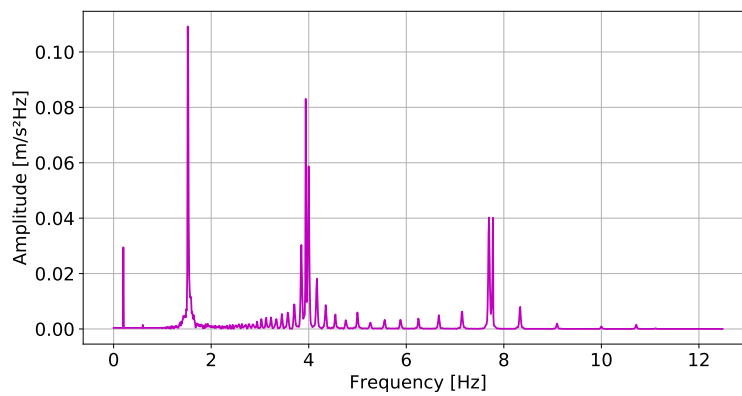


Figure 5.25: Acceleration Amplitude Spectrum of the node at the top of the tower under the action of regular waves ($H_s = 0.3m$, $T_p = 5sec$) & earthquake loads with the presence of hydrodynamic and static radiation damping

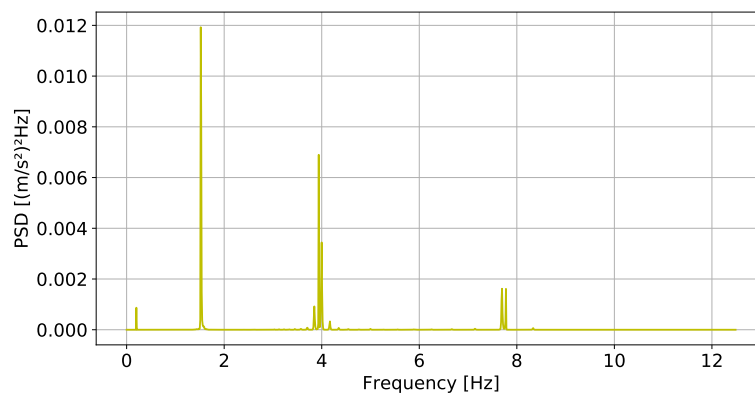


Figure 5.26: Power Spectral Density of the node at the top of the tower under the action of regular waves ($H_s = 0.3m$, $T_p = 5sec$) & earthquake loads with the presence of hydrodynamic and static radiation damping

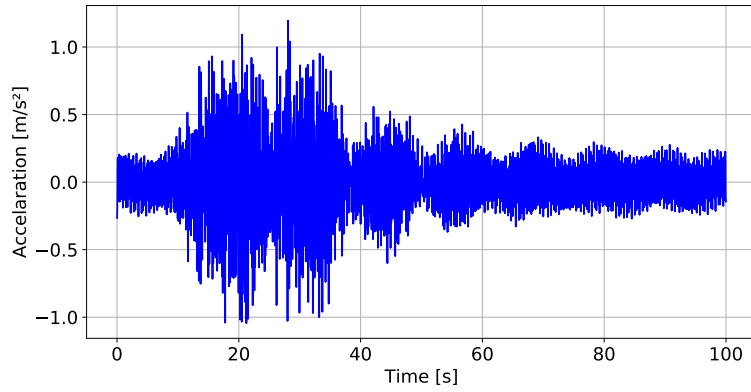


Figure 5.27: Acceleration of the node at the mud line under the action of regular waves ($H_s = 0.3m$, $T_p = 5sec$) & earthquake loads with the presence of hydrodynamic and static radiation damping

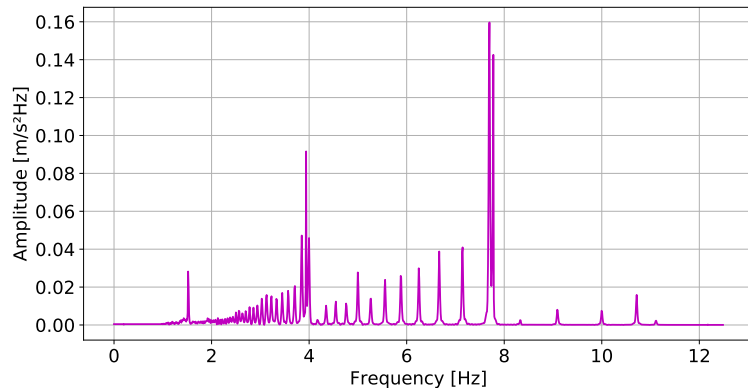


Figure 5.28: Acceleration Amplitude Spectrum of the node at the mud line under the action of regular waves ($H_s = 0.3m$, $T_p = 5sec$) & earthquake loads with the presence of hydrodynamic and static radiation damping

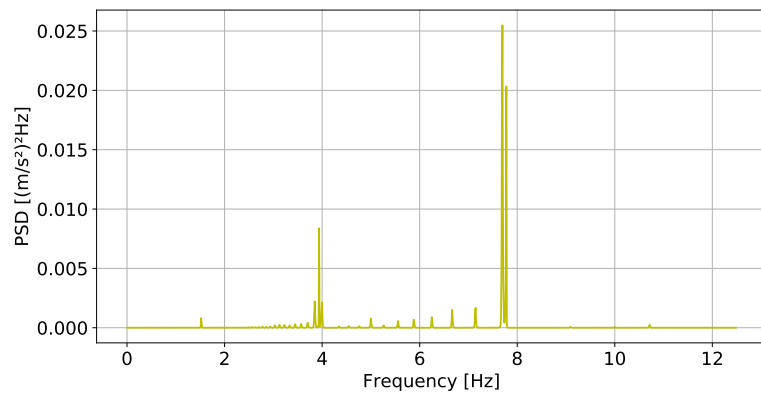


Figure 5.29: Power Spectral Density of the node at the mud line under the action of regular waves ($H_s = 0.3m$, $T_p = 5sec$) & earthquake loads with the presence of hydrodynamic and static radiation damping

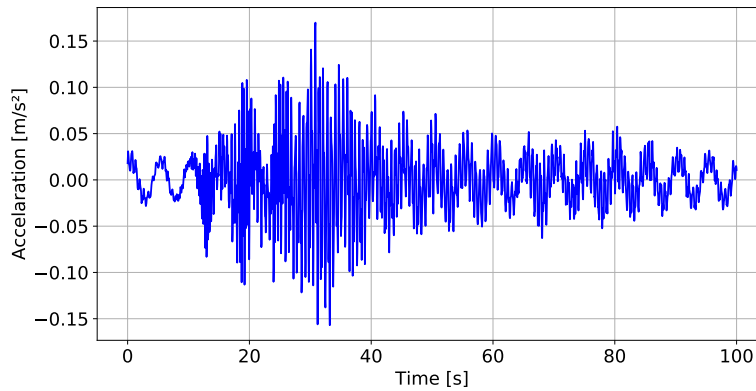


Figure 5.30: Acceleration of the node at the top of the tower under the action of regular waves ($H_s = 0.3m$, $T_p = 5sec$) & earthquake loads with the presence of hydrodynamic and frequency-dependent radiation damping

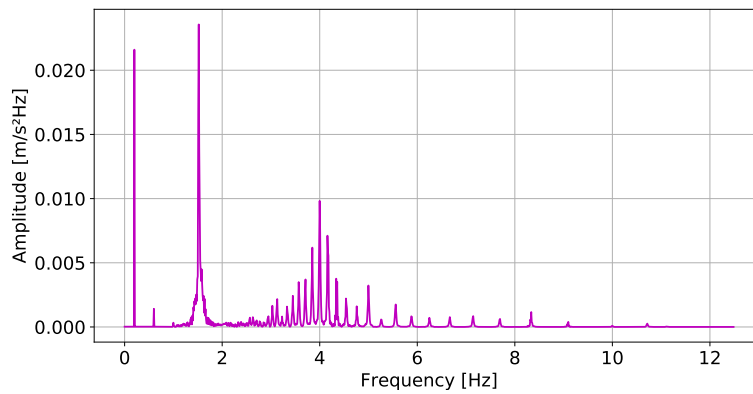


Figure 5.31: Acceleration Amplitude Spectrum of the node at the top of the tower under the action of regular waves ($H_s = 0.3m$, $T_p = 5sec$) & earthquake loads with the presence of hydrodynamic and frequency-dependent radiation damping

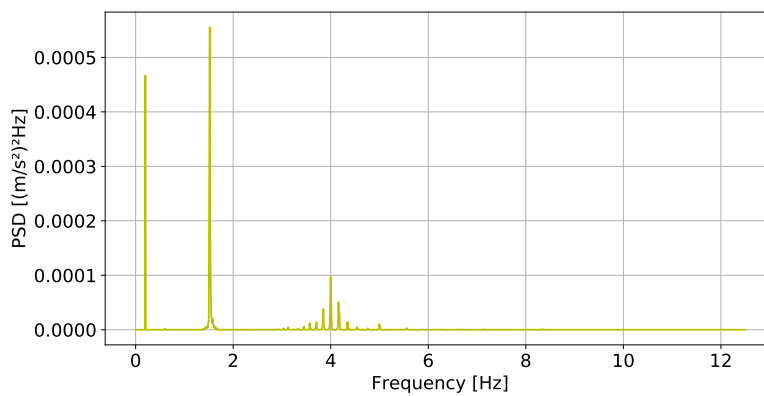


Figure 5.32: Power Spectral Density of the node at the top of the tower under the action of regular waves ($H_s = 0.3m$, $T_p = 5sec$) & earthquake loads with the presence of hydrodynamic and frequency-dependent radiation damping

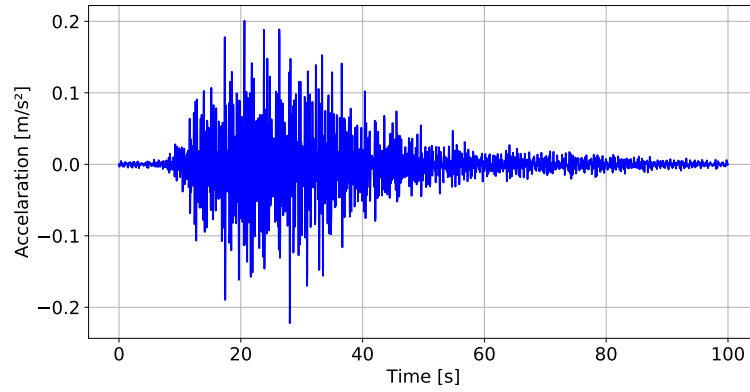


Figure 5.33: Acceleration of the node at the mud line under the action of regular waves ($H_s = 0.3m$, $T_p = 5sec$) & earthquake loads with the presence of hydrodynamic and frequency-dependent radiation damping

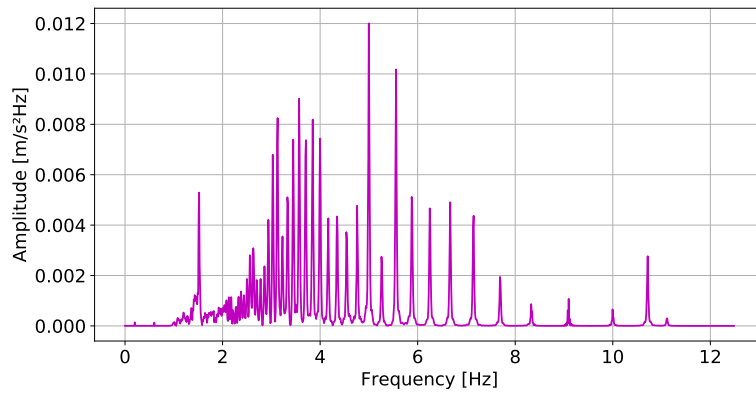


Figure 5.34: Acceleration Amplitude Spectrum of the node at the mud line under the action of regular waves ($H_s = 0.3m$, $T_p = 5sec$) & earthquake loads with the presence of hydrodynamic and frequency-dependent radiation damping

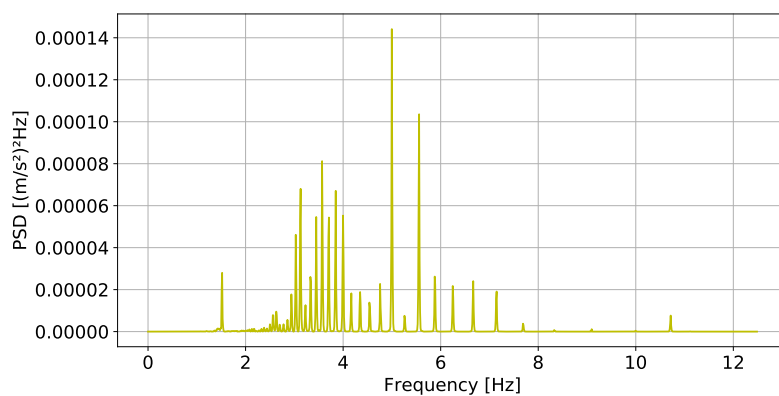


Figure 5.35: Power Spectral Density of the node at the mud line under the action of regular waves ($H_s = 0.3m$, $T_p = 5sec$) & earthquake loads with the presence of hydrodynamic and frequency-dependent radiation damping

5.3.2. Response to Earthquake & Irregular Waves

The analysis of the behavior of the structure under the action of earthquake and irregular waves is of interest for the investigation of the development of the sources of the damping. As in the previous case, the response of the structure is presented for the accelerations.

The time series of the acceleration for the points at the top of the tower and at the mud line are depicted in Figures 5.36 and 5.39 respectively, for the static case. The maximum values for the two cases are decreased considerably when the frequency-dependent dynamic stiffness is active, as it is shown in Figures 5.42 and 5.45.

In the amplitude and PSD spectra for the static case (Figures 5.37 & 5.38) at the top of the tower, it is observed that there is energy concentrated at lower frequencies, possibly because of the presence of the waves. In Figures 5.40 and 5.41 for the mud line, energy is observed at higher frequencies, where the effect of the earthquake is more evident.

The inclusion of the dynamic stiffness matrix influences apparently the response of the structure. Except for the general low deflections at the time-series, a decrease is observed in the results at higher frequencies. The hydrodynamic viscous damping is also present, although it is minor compared with the effect of the soil damping. As in the previous case, the amplitudes at the higher frequencies are close to zero, when the frequency-dependent SSI is included. As an example, in Figure 5.46 there is no peak observed around $8Hz$.

It should be mentioned, that in general the values of the response of the structure are very low when the dynamic stiffness matrix is included. However, the differences in the behaviour of the structure when the frequency-dependent SSI is included, could still be observed.

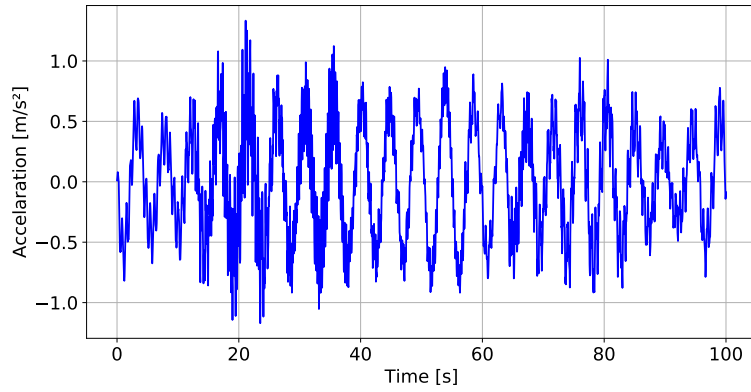


Figure 5.36: Acceleration of the node at the top of the tower under the action of irregular waves ($H_s = 5m$, $T_p = 6sec$) & earthquake loads with the presence of hydrodynamic and static radiation damping

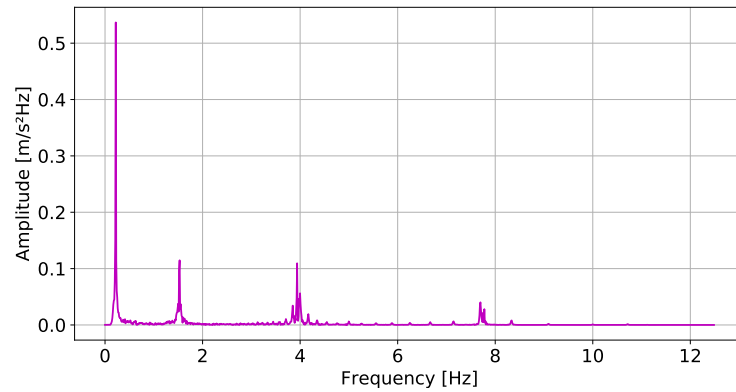


Figure 5.37: Acceleration Amplitude Spectrum of the node at the top of the tower under the action of irregular waves ($H_s = 5m$, $T_p = 6sec$) & earthquake loads, with the presence of hydrodynamic damping and static radiation damping

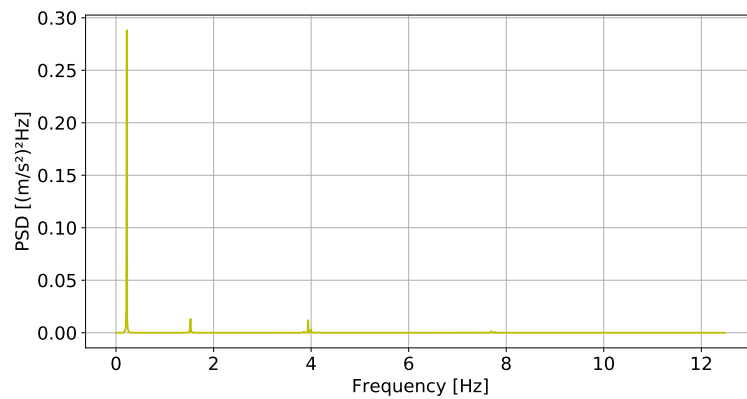


Figure 5.38: Power Spectral Density of the node at the top of the tower under the action of irregular waves ($H_s = 5m$, $T_p = 6sec$) & earthquake loads with the presence of hydrodynamic and static radiation damping

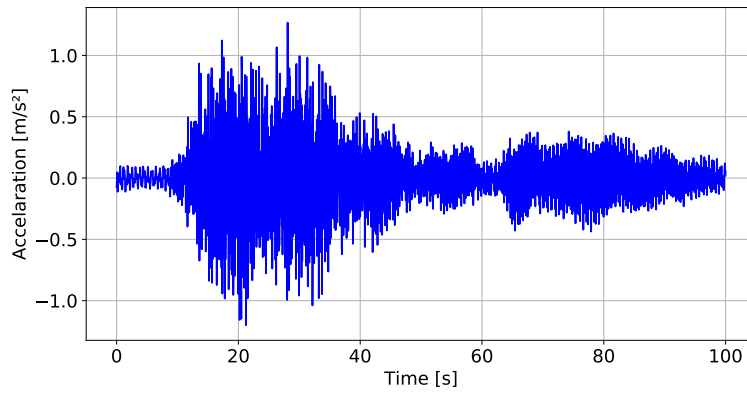


Figure 5.39: Acceleration of the node at the mud line under the action of irregular waves ($H_s = 5m$, $T_p = 6sec$) & earthquake loads with the presence of hydrodynamic and static radiation damping

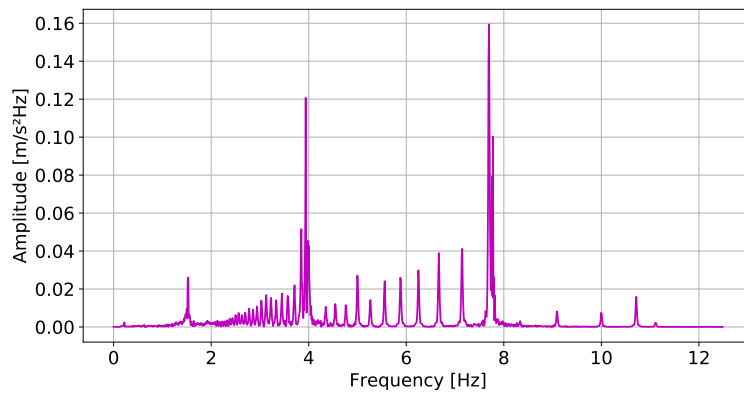


Figure 5.40: Acceleration Amplitude Spectrum of the node at the mud line under the action of irregular waves ($H_s = 5m$, $T_p = 6sec$) & earthquake loads, with the presence of hydrodynamic damping and static radiation damping

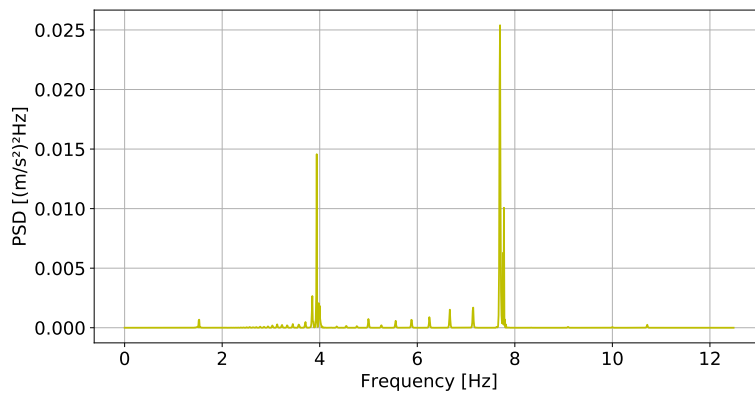


Figure 5.41: Power Spectral Density of the node at the mud line under the action of irregular waves ($H_s = 5m$, $T_p = 6sec$) & earthquake loads with the presence of hydrodynamic and static radiation damping

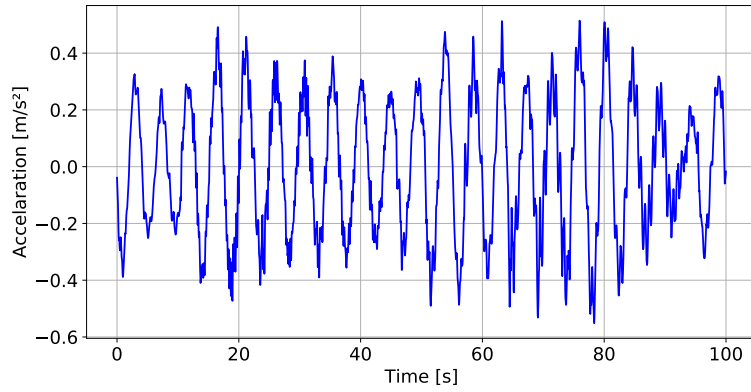


Figure 5.42: Acceleration of the node at the top of the tower under the action of irregular waves ($H_s = 5m$, $T_p = 6sec$) & earthquake loads with the presence of hydrodynamic and frequency-dependent radiation damping

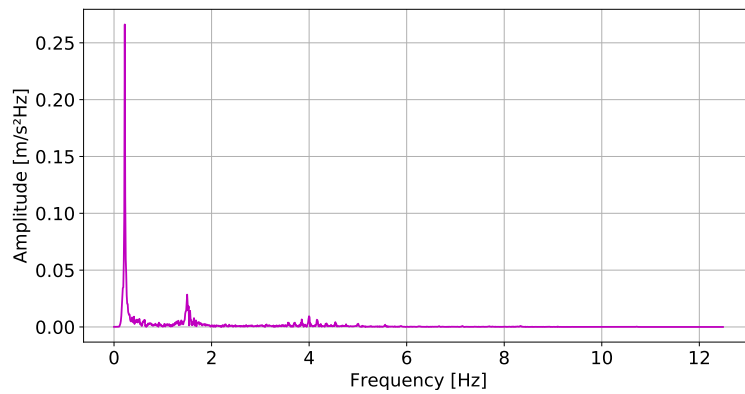


Figure 5.43: Acceleration Amplitude Spectrum of the node at the top of the tower under the action of irregular waves ($H_s = 5m$, $T_p = 6sec$) & earthquake loads, with the presence of hydrodynamic damping and frequency-dependent radiation damping

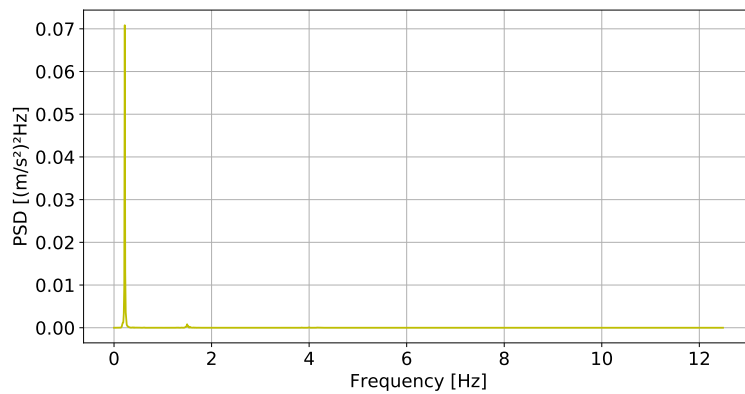


Figure 5.44: Power Spectral Density of the node at the top of the tower under the action of irregular waves ($H_s = 5m$, $T_p = 6sec$) & earthquake loads with the presence of hydrodynamic and frequency-dependent radiation damping

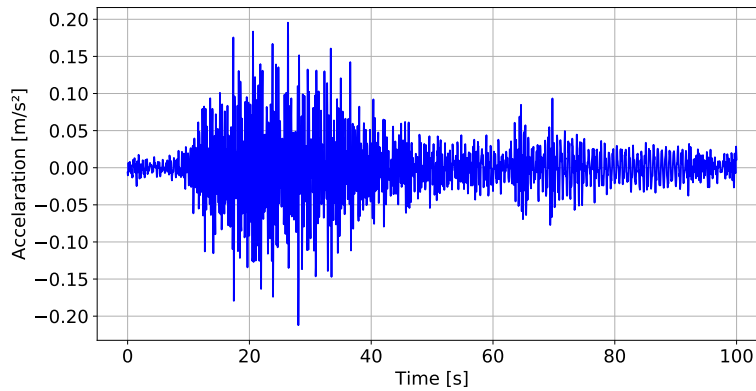


Figure 5.45: Acceleration of the node at the mud line under the action of irregular waves ($H_s = 5m$, $T_p = 6sec$) & earthquake loads with the presence of hydrodynamic and frequency-dependent radiation damping

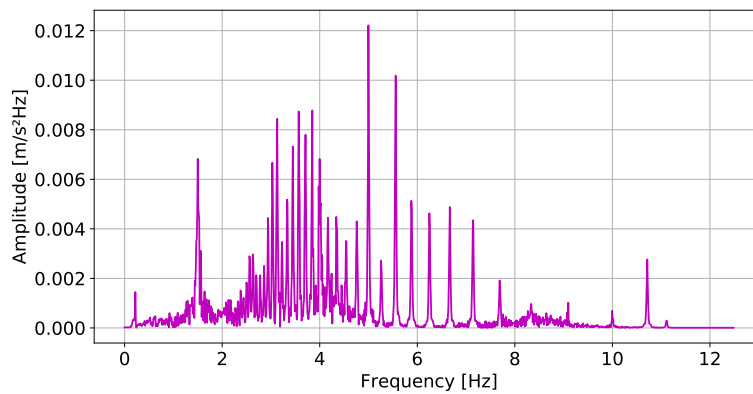


Figure 5.46: Acceleration Amplitude Spectrum of the node at the mud line under the action of irregular waves ($H_s = 5m$, $T_p = 6sec$) & earthquake loads, with the presence of hydrodynamic damping and frequency-dependent radiation damping

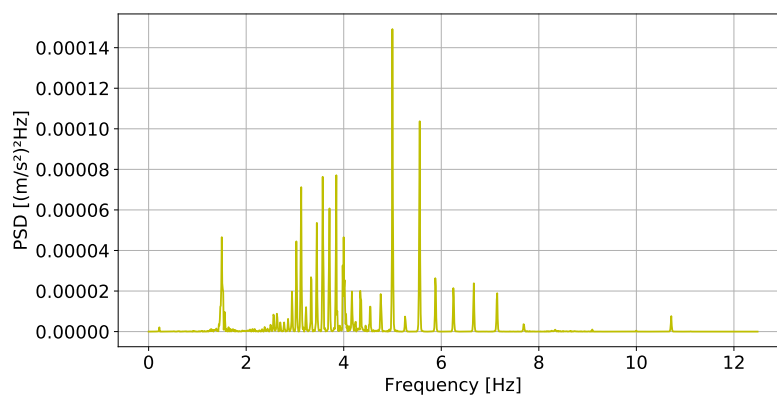


Figure 5.47: Power Spectral Density of the node at the mud line under the action of irregular waves ($H_s = 5m$, $T_p = 6sec$) & earthquake loads with the presence of hydrodynamic and frequency-dependent radiation damping

5.4. Discussion regarding the Sensitivity of the Application of FFT

A general observation in all the results of the applied load cases is that in Figures of the frequency domain, spikes tend to arise, especially at higher frequencies during the presence of earthquake. As the estimation of the responses in the frequency domain is given by the multiplication of the transfer function $H(\omega)$ and the forces $F(\omega)$ for every excitation frequency, the attention goes to the derivation of the excitation forces in the frequency domain. The implementation of FFT for the excitation forces in the frequency domain can lead to inaccuracies in the final result. In Figure 5.48, the single-sided force spectrum is depicted for the simplified case of regular waves at the node at mud line, in order to have a clear understanding about the outcome.

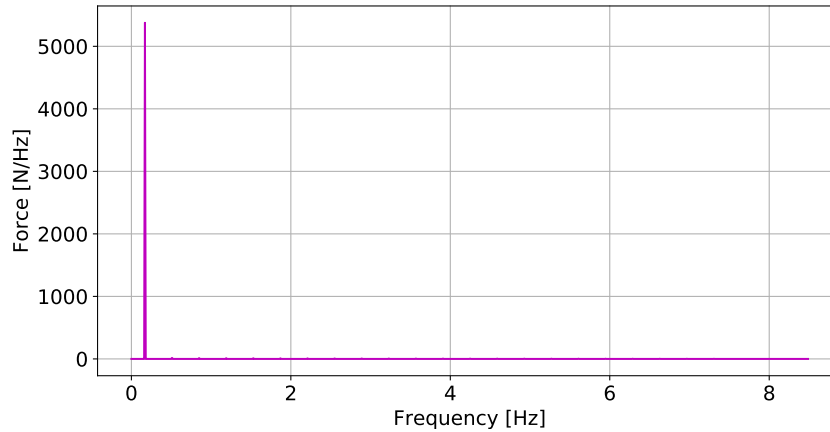


Figure 5.48: Force spectrum for regular waves ($H_s = 5m$, $T_p = 6sec$)

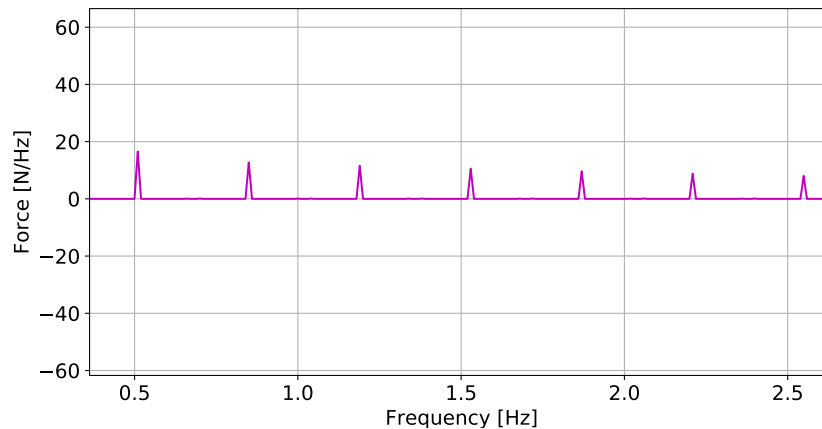


Figure 5.49: Zoomed force spectrum for regular waves ($H_s = 5m$, $T_p = 6sec$)

The peak at the force spectrum should be focused in one frequency, as only regular waves are considered. However, it is observed that there are also spikes close to zero at higher frequencies (Figure 5.49). This indicates that probably the phenomenon of the spectral leakage occurs for the force spectrum, where sharp discontinuities are spread out in the frequency domain [18]. This mainly happens because of the frequency resolution, which is dependent on the length of the signal and the sampling frequency. With the specific frequency resolution, the spectrum can't be represented only at the one peak and energy is leaked to other frequencies as well.

For the derivation of the responses in the frequency domain, the force spectrum is multiplied with the transfer function, which is highly dependent on the frequencies, and this amplifies the final result, especially

during the combined action of hydrodynamic and earthquake loads. In order to avoid the leakage of energy at other frequencies, a larger length of the signal and a different sampling frequency could possibly be selected.

The force spectra for the three tested load cases for the node at mud line are presented at Appendix C.

6

Conclusions & Recommendations for further research

By the conduction of this research for the considered load cases, useful *conclusions* can be drawn:

Initially, a general statement that should be mentioned is that in areas of active seismicity, where the offshore wind turbine structures are under the joint action of multiple loads, the reliable estimation of the dynamic properties, such as the stiffness and the damping, play a crucial role for the analysis of the structural response.

Following the assumption of a non-operational state, the aerodynamic damping, which generally covers the highest percentage of damping to the structure, is not considered. After the study of the rest of the damping sources, it is concluded that the soil damping, and more specifically the radiation soil damping, gives the greatest contribution to the total amount. This generally means that the seismic waves carry away from the structure significant amount of energy. The analysis of the response reveals a damping ratio of around 2.5% for the case of the hydrodynamic loads.

Furthermore, the modelling of the soil-structure interaction with frequency-dependent springs and dampers is of great value for the earthquake engineering and the derivation of the soil radiation damping. However, the estimation of the dynamic stiffness matrix is computationally extensive and requires the analysis of the soil domain. The comparison between the static and the frequency-dependent cases for the soil coefficients indicate the different behaviour of the structure for higher frequencies. During the earthquake action, multiple high frequencies are excited and the frequency-dependent springs and dampers seem to be capable of dissipating the generated energy.

The fact that the dynamic problem is frequency-dependent and the composition of the damping matrix follows a non-classical approach leads to an inefficient solution with the classical methods, that are usually implemented [25]. This holds because the dependency of the frequency requires the solution of the problem in the frequency domain, and additionally, the non diagonal composition of the damping matrix does not establish the modal and eigenvalue analysis suitable for the solution.

Nonetheless, by the applied load case for the hydrodynamic loading, it is concluded that the dynamic stiffness matrix does not affect the results. This happens because the waves are developed in lower frequencies where the soil stiffness is high and the soil damping is lower. The effect of the frequency-dependent soil is more dominant on higher frequencies, where the amplitude spectrum is close to zero.

The application of the three load cases indicates that the hydrodynamic viscous damping does not have compelling consequences on the total response of the offshore wind turbine structure and it is considered much lower comparing to the soil damping. However, for a different case where the natural frequencies could possibly coincide with the wave spectrum, the effect of the hydrodynamic damping could be more evident

for the response of the structure. It should be also mentioned that the hydrodynamic damping does not seem to have a dependency on the frequency.

In spite of that, the estimation of the drag coefficient based on the parameters affecting it, which are also referred at the DNVGL-RP-C205 [10], is a more precise method for the estimation of the hydrodynamic viscous damping and the Morison equation. It should be also highlighted that, as in the most cases the derivation of the hydrodynamic damping is based on experiments, a numerical estimation of it is a further step to its approach.

Based on the outcome of the present master thesis, more questions arise for further investigation leading to the following *recommendations*:

The hydrodynamic viscous damping does not have a significant contribution to the response of the structure for the applied load cases of this thesis. However, the followed approach for the estimation of the hydrodynamic viscous damping and the drag coefficient should be also implemented for different cases of the hydrodynamic loads and for other types of offshore structure (jacket etc.), in order to study the influence on the results.

The effect of the surface roughness should also be of importance for the reliable estimation of the drag coefficient, and respectively of the hydrodynamic viscous damping. This could be achieved by analyzing it with the aid of Computational Fluid Dynamics.

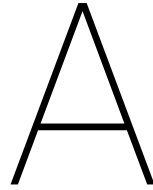
For the present thesis, the already existing soil model was added in order to represent the soil-structure interaction with many simplifications. However, the soil model could be further improved to represent more analytically the soil profile.

The accuracy of the estimation of the excitation seismic force should be investigated further. It should also consider the variations of the depth and be applied on the strings and the dampers and not directly on the nodes of the monopile.

Furthermore, the composition of the total damping matrix should also be further improved to represent all the sources of damping. The aerodynamic damping could also be accounted by applying load cases with the aerodynamic loads included. A better representation of the structural damping, especially in direct analysis, has also to be investigated.

The applicability of the Inverse Fast Fourier transform should be examined in detail to avoid possible errors in the results in the frequency domain. Measurements should also be taken in order to mitigate the effect of spectral leakage. For instance, the total time interval and the sampling frequency seem to be very crucial parameters to be checked.

Finally, the soil radiation damping seems crucial for the dissipation of the energy of the structure under the action of earthquake loads. As there is limited reference of it in the literature, it should be examined further if it could lead to a more economical design of offshore wind turbine structures in areas of active seismicity.



Details of Structure

In this Appendix the relevant information concerning the structure and its properties is presented.

Part of the Structure	Material	E[Pa]	ν	$\rho[kg/m^3]$
Foundation	S355	$2.1 * 10^{11}$	0.3	7850
Tower	S355	$2.1 * 10^{11}$	0.3	7952

Table A.1: Material Properties of the Structure

The mass representing the rotor nacelle assembly is equal to 500000kg.

Element	Diameter top [m]	Diameter bottom [m]	thickness [m]	z (+LAT) [m]
1	6.5	6.5	0.065	19
2	6.5	6.5	0.065	18
3	6.5	6.5	0.065	17
4	6.5	6.5	0.065	16
5	6.5	6.5	0.065	15
6	6.5	6.5	0.065	14
7	6.5	6.5	0.065	13
8	6.5	6.5	0.065	12
9	6.5	6.5	0.065	11
10	6.5	6.5	0.065	10
11	6.5	6.5	0.065	9
12	6.5	6.5	0.065	8
13	6.5	6.5	0.065	7
14	6.5	6.5	0.065	6
15	6.5	6.5	0.065	5
16	6.5	6.5	0.065	4
17	6.5	6.5	0.065	3
18	6.5	6.5	0.065	2
19	6.5	6.5	0.065	1
20	6.5	6.5	0.065	0

Table A.2: Details of the Foundation above mud line

Element	Diameter top [m]	Diameter bottom [m]	thickness [m]	z (+LAT) [m]
21	6.5	6.5	0.065	-1
22	6.5	6.5	0.065	-2
23	6.5	6.5	0.065	-3
24	6.5	6.5	0.065	-4
25	6.5	6.5	0.065	-5
26	6.5	6.6	0.065	-6
27	6.6	6.7	0.066	-7
28	6.7	6.8	0.067	-8
29	6.8	6.9	0.068	-9
30	6.9	7	0.069	-10
31	7	7.1	0.07	-11
32	7.1	7.2	0.071	-12
33	7.2	7.3	0.072	-13
34	7.3	7.4	0.073	-14
35	7.4	7.5	0.074	-15
36	7.5	7.5	0.075	-16
37	7.5	7.5	0.075	-17
38	7.5	7.5	0.075	-18
39	7.5	7.5	0.075	-19
40	7.5	7.5	0.075	-20
41	7.5	7.5	0.075	-21
42	7.5	7.5	0.075	-22
43	7.5	7.5	0.075	-23
44	7.5	7.5	0.075	-24
45	7.5	7.5	0.075	-25
46	7.5	7.5	0.075	-26
47	7.5	7.5	0.075	-27
48	7.5	7.5	0.075	-28
49	7.5	7.5	0.075	-29
50	7.5	7.5	0.075	-30
51	7.5	7.5	0.075	-31
52	7.5	7.5	0.075	-32
53	7.5	7.5	0.075	-33
54	7.5	7.5	0.075	-34
55	7.5	7.5	0.075	-35
56	7.5	7.5	0.075	-36
57	7.5	7.5	0.075	-37
58	7.5	7.5	0.075	-38
59	7.5	7.5	0.075	-39
60	7.5	7.5	0.075	-40
61	7.5	7.5	0.075	-41
62	7.5	7.5	0.075	-42
63	7.5	7.5	0.075	-43
64	7.5	7.5	0.075	-44
65	7.5	7.5	0.075	-45
66	7.5	7.5	0.075	-46
67	7.5	7.5	0.075	-47
68	7.5	7.5	0.075	-48
69	7.5	7.5	0.075	-49
70	7.5	7.5	0.075	-50
71	7.5	7.5	0.075	-51
72	7.5	7.5	0.075	-52
73	7.5	7.5	0.075	-53
74	7.5	7.5	0.075	-54
75	7.5	7.5	0.075	-55
76	7.5	7.5	0.075	-56
77	7.5	7.5	0.075	-57

Table A.3: Details of the Foundation below mud line

Element	Diameter top [m]	Diameter bottom [m]	thickness [m]	z (+LAT) [m]
1	4.61	4.53	0.100	111.00
2	4.53	4.53	0.025	110.87
3	4.53	4.53	0.025	110.77
4	4.53	4.53	0.025	110.67
5	4.53	4.53	0.024	109.91
6	4.53	4.53	0.024	109.88
7	4.53	4.53	0.024	109.80
8	4.53	4.53	0.024	109.72
9	4.53	4.59	0.020	109.69
10	4.59	4.67	0.016	107.58
11	4.67	4.76	0.016	104.82
12	4.76	4.84	0.016	102.07
13	4.84	4.93	0.016	99.32
14	4.93	5.01	0.017	96.57
15	5.01	5.10	0.017	93.83
16	5.10	5.18	0.018	91.09
17	5.18	5.27	0.019	88.35
18	5.27	5.35	0.020	85.62
19	5.35	5.44	0.020	82.89
20	5.44	5.52	0.021	80.16
21	5.52	5.52	0.021	77.44
22	5.52	5.52	0.021	77.41
23	5.52	5.52	0.021	77.32
24	5.52	5.52	0.021	77.23
25	5.52	5.54	0.021	77.20
26	5.54	5.62	0.022	76.56
27	5.62	5.70	0.022	73.82
28	5.70	5.78	0.023	71.09
29	5.78	5.86	0.023	68.36
30	5.86	5.94	0.024	65.63
31	5.94	6.02	0.024	62.91
32	6.02	6.10	0.024	60.18
33	6.10	6.17	0.025	57.46
34	6.17	6.25	0.025	54.75
35	6.25	6.33	0.025	52.03
36	6.33	6.41	0.026	49.32
37	6.41	6.49	0.026	46.62
38	6.49	6.49	0.026	43.90
39	6.49	6.49	0.026	43.87
40	6.49	6.49	0.026	43.76
41	6.49	6.49	0.026	43.65
42	6.49	6.49	0.026	43.62
43	6.49	6.49	0.027	41.62
44	6.49	6.49	0.027	38.67
45	6.49	6.49	0.028	34.38
46	6.49	6.50	0.031	30.09
47	6.50	6.50	0.038	27.16
48	6.50	6.50	0.038	25.66
49	6.50	6.50	0.038	22.73
50	6.50	6.50	0.038	19.80
51	6.50	6.50	0.038	19.18
52	6.50	6.50	0.038	19.14

Table A.4: Details of the Tower

B

Estimation of the Drag Coefficient

In Chapter 4, an example for the variation of the drag coefficient is presented, for irregular waves with $H_s = 5m$ and $T_p = 6sec$. The estimated values are shown in Table B.1 in detail.

Diameter [m]	Δ	C_{ds}	KC number	ψ	C_d	$\sigma [m/s]$	Hydro. damp. coefficient
6.5	7.69231E-07	0.65	5.987	0.696	0.452	1.012	2431.905
6.5	7.69231E-07	0.65	4.940	0.591	0.384	1.219	2489.375
6.5	7.69231E-07	0.65	3.901	0.487	0.317	0.815	1371.455
6.5	7.69231E-07	0.65	3.385	0.435	0.283	0.882	1327.101
6.5	7.69231E-07	0.65	2.371	0.334	0.217	0.908	1048.384
6.5	7.69231E-07	0.65	2.117	0.309	0.201	0.937	998.781
6.5	7.69231E-07	0.65	1.921	0.297	0.193	0.849	871.202
6.5	7.69231E-07	0.65	1.732	0.297	0.193	0.739	758.573
6.5	7.69231E-07	0.65	1.556	0.297	0.193	0.649	665.584
6.5	7.69231E-07	0.65	1.395	0.297	0.193	0.573	587.417
6.5	7.69231E-07	0.65	1.251	0.297	0.193	0.508	520.903
6.6	7.57576E-07	0.65	1.104	0.297	0.193	0.452	470.953
6.7	7.46269E-07	0.65	0.976	0.297	0.193	0.404	427.272
6.8	7.35294E-07	0.65	0.864	0.297	0.193	0.362	388.907
6.9	7.24638E-07	0.65	0.766	0.297	0.193	0.326	355.116
7	7.14286E-07	0.65	0.681	0.435	0.283	0.294	476.853
7.1	7.04225E-07	0.65	0.607	0.584	0.379	0.267	587.857
7.2	6.94444E-07	0.65	0.542	0.713	0.463	0.243	662.274
7.3	6.84932E-07	0.65	0.486	0.825	0.536	0.222	709.723
7.4	6.75676E-07	0.65	0.437	0.922	0.600	0.203	737.700
7.5	6.66667E-07	0.65	0.395	1.007	0.654	0.187	751.981
7.5	6.66667E-07	0.65	0.364	1.070	0.695	0.174	740.347
7.5	6.66667E-07	0.65	0.336	1.124	0.731	0.162	724.993
7.5	6.66667E-07	0.65	0.313	1.171	0.761	0.152	707.981
7.5	6.66667E-07	0.65	0.293	1.210	0.787	0.143	690.835
7.5	6.66667E-07	0.65	0.277	1.243	0.808	0.136	674.656
7.5	6.66667E-07	0.65	0.264	1.270	0.825	0.130	660.213
7.5	6.66667E-07	0.65	0.255	1.287	0.836	0.126	646.080
7.5	6.66667E-07	0.65	0.249	1.298	0.844	0.123	634.945
7.5	6.66667E-07	0.65	0.245	1.306	0.849	0.121	627.479
7.5	6.66667E-07	0.65	0.244	1.310	0.851	0.119	623.734

Table B.1: Values for the variation of the drag coefficient

C

Force Spectra

The force spectra for the three tested load cases for the point at mud line are presented in the following Figures:

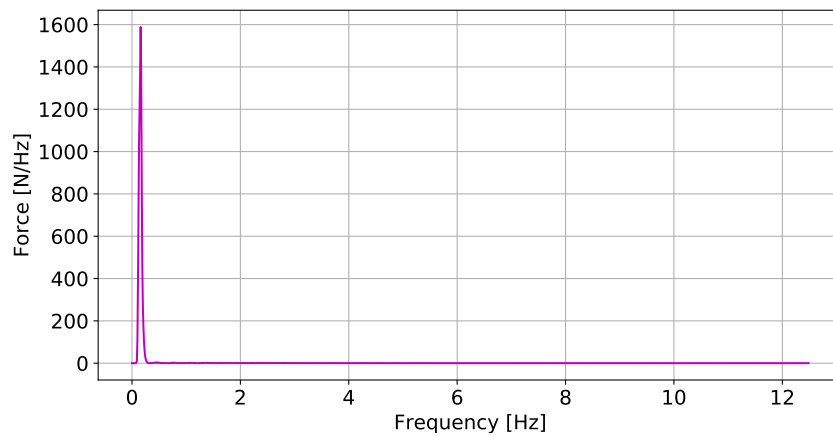


Figure C.1: Force spectrum for irregular waves ($H_s = 5m$, $T_p = 6sec$)

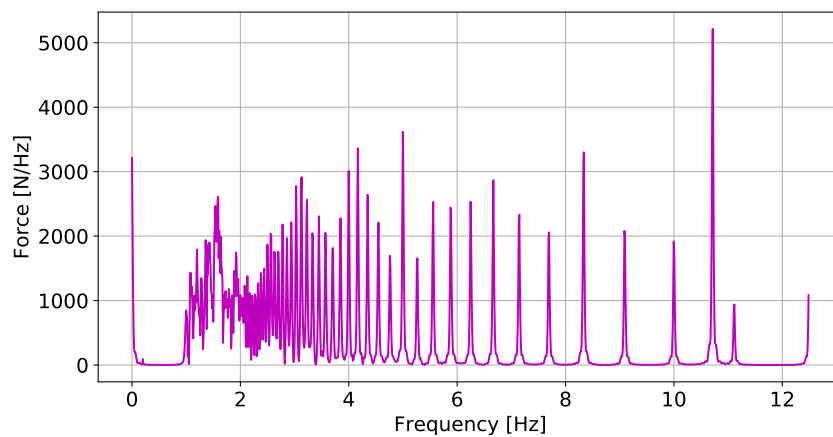


Figure C.2: Force spectrum for regular waves ($H_s = 0.3m$, $T_p = 5sec$) and earthquake

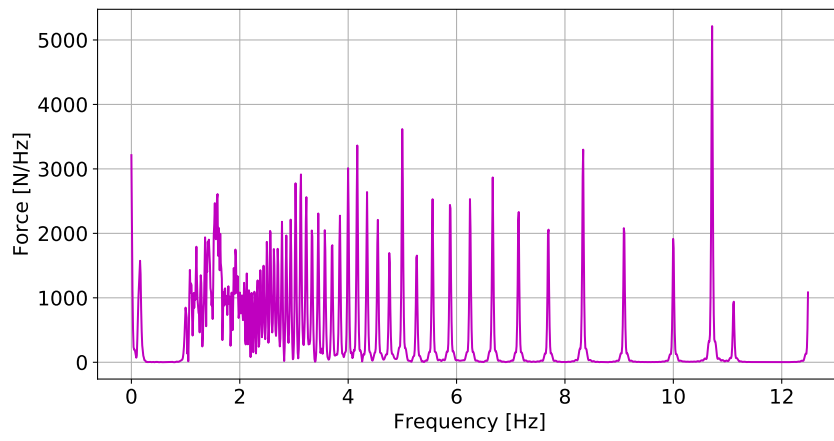


Figure C.3: Force spectrum for irregular waves ($H_s = 5m$, $T_p = 6sec$) and earthquake

Bibliography

- [1] Nyquist–Shannon sampling theorem. *Wikipedia: The Free Encyclopedia*. URL https://en.wikipedia.org/wiki/Nyquist%E2%80%93Shannon_sampling_theorem.
- [2] Spectral density. *Wikipedia: The Free Encyclopedia*. URL https://en.wikipedia.org/wiki/Spectral_density#Power_spectral_density.
- [3] Taiwan: pursuing a new green energy revolution in the East. *POWER TECHNOLOGY*, 2018. URL <https://www.power-technology.com/features/taiwan-pursuing-new-green-energy-revolution-east/>.
- [4] M. ASCE Anestis S. Veletsos and S. M. ASCE Carlos E. Ventura. Dynamic analysis of structures by the DFT method. I(12):2625–2642, 1986.
- [5] P. W. RUSSELL BEARMAN. Measurements of Hydrodynamic Damping of Bluff Bodies with Application to the Prediction of Viscous Damping of TLP Hulls. *21st Symposium On Naval Hydrodynamics, Trondheim, Norway*, pages 61–73, 1996.
- [6] Li Bin, Peco Christian, Millan Daniel, Arias Irene, and Arroyo Marino. Phase-field modeling and simulation of fracture in brittle materials with strongly anisotropic surface energy. *International Journal for Numerical Methods in Engineering*, (1):343–352, 2014. ISSN 0743-1619. doi: 10.1002/nme.
- [7] Indrajit Chowdhury, Chief Discipline Supervisor, Structural Engineering, Petrofac International Limited, and Shambhu P Dasgupta. Computation of Rayleigh Damping Coefficients for Large Systems Computation of Rayleigh Damping Coefficients for Large Systems. (January 2003), 2016.
- [8] Craig Richard. Taiwan sets out 5.5GW plan. *WINDPOWER OFFSHORE*, 2018. URL <https://www.windpoweroffshore.com/article/1462340/taiwan-sets-55gw-plan>.
- [9] M. Damgaard, L. B. Ibsen, L. V. Andersen, and J. K.F. Andersen. Cross-wind modal properties of offshore wind turbines identified by full scale testing. *Journal of Wind Engineering and Industrial Aerodynamics*, 116:94–108, 2013. ISSN 01676105. doi: 10.1016/j.jweia.2013.03.003. URL <http://dx.doi.org/10.1016/j.jweia.2013.03.003>.
- [10] DNV GL - Det Norske Veritas Germanischer Lloyd. DNVGL-RP-C205: Environmental Conditions and Environmental Loads. *DNV GL Recommended Practice*, (August):1–259, 2017.
- [11] Patrick Guillaume, Gert De Sitter, Pieter Jan Jordaens, and Christof Devriendt. Damping estimation of an offshore wind turbine on a monopile foundation. *IET Renewable Power Generation*, 7(4):401–412, 2013. ISSN 1752-1416. doi: 10.1049/iet-rpg.2012.0276. URL <https://digital-library.theiet.org/content/journals/10.1049/iet-rpg.2012.0276>.
- [12] J. Mark F.G. Holst, J. Michael Rotter, Chris R. Calladine, Eoin Dunphy, EUROPEAN STANDARD NORME EUROPEENNE EUROPEAN NORM, DNV, E C Carvalho, Chairman T C Sc, Oung Park, Raphael T Haftka, Bhavani V Sankar, and James H Starnes. H E U R O P E a n N I O N. *Journal of Constructional Steel Research*, 54(2):18–20, 2011. ISSN 00218669. doi: 10.2514/2.2772.
- [13] Leo H. Holthuijsen. *Waves in Oceanic and Coastal Waters*. Cambridge University Press, Cambridge, 2007. ISBN 9780511618536. doi: 10.1017/CBO9780511618536. URL <http://ebooks.cambridge.org/ref/id/CBO9780511618536>.
- [14] C Ouled Housseine, C Monroy, and F Bigot. A new linearization method for vectorial Morison equation. 2(April):1–4, 2015.

- [15] L. Johanning, P. W. Bearman, and J. M.R. Graham. Hydrodynamic damping of a large scale surface piercing circular cylinder in planar oscillatory motion. *Journal of Fluids and Structures*, 2001. ISSN 08899746. doi: 10.1006/jfls.2001.0388.
- [16] Coordination P Kotronis, Claudio Tamagnini, Stéphane Grange, Panagiotis Kotronis, Claudio Tamagnini, and Stéphane Grange. ALERT Doctoral School 2013, Soil-Structure Interaction. (October):2013, 2013. ISSN 2954251743.
- [17] Christina Koukoura, Anand Natarajan, and Allan Vesth. Identification of support structure damping of a full scale offshore wind turbine in normal operation. *Renewable Energy*, 81:882–895, 2015. ISSN 18790682. doi: 10.1016/j.renene.2015.03.079. URL <http://dx.doi.org/10.1016/j.renene.2015.03.079>.
- [18] Mathuranathan. FFT and Spectral Leakage. *GaussianWaves*, 2011. URL <https://www.gaussianwaves.com/2011/01/fft-and-spectral-leakage-2/>.
- [19] Zsuzsa B Pap and László P Kollár. Effect of Resonance in Soil-Structure Interaction for Finite Soil Layers. *Periodica Polytechnica Civil Engineering*, pages 1–9, 2018. ISSN 0553-6626. doi: 10.3311/ppci.11960.
- [20] Turgut Sarp Sarpkaya. *Wave forces on offshore structures*. 2012. ISBN 9781139195898. doi: 10.1017/CBO9781139195898.
- [21] Gangsig Shin and Ohseop Song. A Time-Domain Method to Generate Artificial Time History from a Given Reference Response Spectrum. *Nuclear Engineering and Technology*, 48(3):831–839, 2016. ISSN 2234358X. doi: 10.1016/j.net.2016.01.023. URL <http://dx.doi.org/10.1016/j.net.2016.01.023>.
- [22] R. Shirzadeh, C. Devriendt, M. A. Bidakhvidi, and P. Guillaume. Experimental and computational damping estimation of an offshore wind turbine on a monopile foundation. *Journal of Wind Engineering and Industrial Aerodynamics*, 120:96–106, 2013. ISSN 01676105. doi: 10.1016/j.jweia.2013.07.004. URL <http://dx.doi.org/10.1016/j.jweia.2013.07.004>.
- [23] Mathematical Statistics. Random Hydrodynamic Forces on Objects Author (s): Leon E. Borgman Source : The Annals of Mathematical Statistics , Vol . 38 , No . 1 (Feb ., 1967), pp . 37-51 Published by : Institute of Mathematical Statistics Stable URL : [https://www.jstor.org/stab.38\(1\):37-51](https://www.jstor.org/stab.38(1):37-51), 2019.
- [24] George Gabriel Stokes and George Gabriel Stokes. On the Effect of the Internal Friction of Fluids on the Motion of Pendulums. In *Mathematical and Physical Papers*, pages 1–10. Cambridge University Press, 8 2010. doi: 10.1017/cbo9780511702266.002.
- [25] Dynamics O F Structures. *DYNAMICS OF STRUCTURES Theory and Applications to Earthquake Engineering Anil K. Chopra University*. ISBN 9780132858038.
- [26] A Tsouvalas. Lecture notes CIE5260 Structural Response to Earthquakes Seismic - Analysis of Complex Structures. page 341, 2017.
- [27] W. G. Versteijlen, J. M. de Oliveira Barbosa, K. N. van Dalen, and A. V. Metrikine. Dynamic soil stiffness for foundation piles: Capturing 3D continuum effects in an effective, non-local 1D model. *International Journal of Solids and Structures*, 134:272–282, 2018. ISSN 00207683. doi: 10.1016/j.ijsolstr.2017.11.007. URL <https://doi.org/10.1016/j.ijsolstr.2017.11.007>.
- [28] Chang-Yi Wang. On high-frequency oscillatory viscous flows. *Journal of Fluid Mechanics*, 32(1):55–68, 4 1968. ISSN 0022-1120. doi: 10.1017/S0022112068000583. URL https://www.cambridge.org/core/product/identifier/S0022112068000583/type/journal_article.
- [29] Xiang Yuan Zheng, Hongbin Li, Weidong Rong, and Wei Li. Joint earthquake and wave action on the monopile wind turbine foundation: An experimental study. *Marine Structures*, 44:125–141, 2015. ISSN 09518339. doi: 10.1016/j.marstruc.2015.08.003.